Journal of Inorganic Biochemistry 231 (2022) 111790

Contents lists available at ScienceDirect

Journal of Inorganic Biochemistry

journal homepage: www.elsevier.com/locate/jinorgbio

Rational design of mitochondria targeted thiabendazole-based Ir(III) biscyclometalated complexes for a multimodal photodynamic therapy of cancer

Igor Echevarría [a], Elisenda Zafon [b], Sílvia Barrabés [b], María Ángeles Martínez [c], Sonia Ramos-Gómez [e], Natividad Ortega [e], Blanca R. Manzano [d], Félix A. Jalón [d], Roberto Quesada [a], Gustavo Espino [a,*], Anna Massaguer [b,*]

[a] Universidad de Burgos, Departamento de Química, Facultad de Ciencias, Plaza Misael Bañuelos s/n, 09001 Burgos, Spain
[b] Universitat de Girona, Departament de Biologia, Facultat de Ciències, Maria Aurelia Capmany 40, 17003 Girona, Spain
[c] Universitat de Girona, Departament de Química, Facultat de Ciències, Maria Aurelia Capmany 40, 17003 Girona, Spain
[d] Universidad de Castilla-La Mancha, Departamento de Química Inorgánica, Orgánica y Bioquímica. Facultad de Ciencias y Tecnologías Químicas, Avda. Camilo J. Cela 10, 13071 Ciudad Real, Spain
[e] Universidad de Burgos, Departamento de Biotecnología y Ciencia de los Alimentos, Facultad de Ciencias

ARTICLE INFO

Keywords:
Photodynamic therapy
Iridium
Cyclometalated complexes
Cancer
Mitochondria
DNA

ABSTRACT

Despite their outstanding properties as potential photosensitizers for photodynamic therapy (PDT), Ir(III) biscyclometalated complexes need both further developments to overcome remaining limitations and in-depth investigations into their mechanisms of action to reach clinic application in the treatment of cancer. This work describes the synthesis of a family of Ir(III) complexes of general formula $[Ir(C^N)_2(N^N')]Cl$ (N^N′ = thiabendazole-based ligands; C^N = ppy (2-phenylpyridinate) (Series A), or dfppy (2-(2,4-difluorophenyl)pyridinate) (Series B)) and their evaluation as potential PDT agents. These complexes are partially soluble in water and exhibit cytotoxic activity in the absence of light irradiation versus several cancer cell lines. Furthermore, the cytotoxic activity of derivatives of Series A is enhanced upon irradiation, particularly for complexes **[1a]Cl** and **[3a]Cl**, which show phototoxicity indexes (PI) above 20. Endocytosis was established as the uptake mechanism for **[1a]Cl** and **[3a]Cl** in prostate cancer cells by flow cytometry. These derivatives mainly accumulate in the mitochondria as shown by colocalization confocal microscopy experiments. Presumably, **[1a]Cl** and **[3a]Cl** induce death on cancer cells under irradiation through apoptosis triggered by a multimodal mechanism of action, which likely involves damage over mitochondrial DNA and mitochondrial membrane depolarization. Both processes seem to be the result of photocatalytic oxidation processes.

1. Introduction

Photodynamic therapy (PDT) is a non-invasive chemotherapeutic protocol indicated for the treatment of non-oncological diseases and some cancer types. It is based on the administration of a photosensitive compound called photosensitizer (PS), whose excitation by irradiation with light specifically directed towards the malignant tissue triggers the photochemical generation of reactive oxygen species (ROS) from cellular O_2, and subsequently causes death on cancer cells. It features some inherent advantages, such as reduced side-effects based on selective photoactivation of the drug on cancer tissues (i.e.: improved selectivity), diminished acquired resistance of cancer cells stemming

Abbreviations: CV, Cyclic voltammetry; DPBF, 1,3-Diphenylisobenzofuran; DMEM, Dulbecco's modified Eagle's medium; dfppy, 2-(2,4-difluorophenyl)pyridinate; DFT, Density functional theory; EDTA, Ethylenediaminetetraacetic acid; FBS, Fetal bovine serum; HOMO, Highest Occupied Molecular Orbital; IC_{50}, Half maximal inhibitory concentration; LUMO, Lowest Unoccupied Molecular Orbital; MFI, Median fluorescence intensity; MMP, Mitochondrial membrane potential; mtDNA, Mitochondrial DNA; NAD, Nicotinamide adenine dinucleotide; NIR, Near-infrared; PBS, Phosphate Buffer Saline; PDT, Photodynamic therapy; PEG, Polyethylene glycol; PI, Phototoxicity index; ppy, 2-phenylpyridinate; PS, Photosensitizer; ROS, Reactive oxygen species; SC, Supercoiled conformation; SPI, Selective Phototoxicity Index; TD-DFT, Time-dependent density functional theory.

* Corresponding authors.
E-mail addresses: gespino@ubu.es (G. Espino), anna.massaguer@udg.edu (A. Massaguer).

https://doi.org/10.1016/j.jinorgbio.2022.111790
Received 18 November 2021; Received in revised form 25 February 2022; Accepted 7 March 2022
Available online 14 March 2022
0162-0134/© 2022 The Authors. Published by Elsevier Inc. This is an open access article under the CC BY-NC-ND license (http://creativecommons.org/licenses/by-nc-nd/4.0/).

from their multiple cellular targets and mechanisms of action (i.e.: enhanced efficiency), and a broad spectrum of treatable cancer types [1–4].

Ir(III) biscyclometalated complexes are under investigation as promising PDT agents for the treatment of different cancer types due to their remarkable photophysical properties [5–8]. In particular, their strong spin-orbit coupling constant favours the access to a triplet excited state that can interact with molecular oxygen in the cells to produce ROS through either an electron transfer pathway (superoxide radical anion, $O_2^{\bullet-}$) or an energy transfer mechanism (singlet oxygen, $^1O_2$). More importantly, these processes are photocatalytic in nature, which potentially leads to a very efficient therapeutic activity and allows decreasing the PS dosage [5,9–11]. Several additional features will condition the potential applicability of selected Ir-based PSs in specific clinical PDT protocols. Among these desired features it is worth mentioning the following: (1) reasonable aqueous solubility to facilitate administration, (2) straightforward synthetic procedures to reduce costs, (3) good photostability and phototoxicity indexes (PI = $IC_{50,dark}$/$IC_{50,light}$) to ensure a selective photo-enhanced activity and (4) suitable absorption profiles in relation to the cancer type to be treated, that is, blue light-sensitive PSs can be used to treat superficial or cutaneous cancers but near infrared (NIR) or red light-sensitive PSs are needed to deal with tumours on internal tissues, due to the higher tissue penetration of this type of light stimulus [12–14]. Nonetheless, this determinant can be bypassed to some extent using two-photon excitation PDT [15] or employing endoscopic light delivery devices based on laser or light emitting diode (LED) optical fibers [16].

Recently, several researching groups have reported encouraging advances in the field of Ir(III) PSs for PDT. For instance, the group of Huang has described a tricationic Ir(III) PS with high phototoxicity in both in vitro cancer cell lines and in vivo mouse cancer models and high photocatalytic activity on the oxidation of the reduced form of nicotinamide adenine dinucleotide (NADH), nicotinamide adenine dinucleotide phosphate (NADPH) and amino acids [17]. Gou et al. have reported an Ir(III) complex containing a Donor-Acceptor-Donor ligand that can be directly promoted to the excited state by NIR radiation to produce ROS and heat, so that it exhibits a dual phototherapeutic action, i.e. photodynamic therapy plus photothermal therapy. In addition, this complex has been conjugated to polyethylene glycol (PEG) to generate highly soluble nanoparticles and display a significant tumour inhibition in vivo [18]. The group of He has prepared an Ir(III) complex that features high PI values in different cancer cell lines and multicellular spheroids under hypoxia through a synergistic effect between ferroptosis and apoptosis, induced by the generation of the radicals superoxide ($O_2^{\bullet-}$) and hydroxyl ($^{\bullet}OH$) [19]. The group of Bryce has rationally designed two Ir-porphyrin conjugates that show synergistic PDT-photothermal activity under long-wavelength excitation (635 nm) [20].

Many of the PSs currently in clinical or pre-clinical studies localize in or have a major influence on mitochondria, promoting a PDT induced apoptotic cell death [21]. Mitochondria are considered as the powerhouses of cells, in as much as they produce energy in the form of adenosine triphosphate (ATP) through different biochemical processes such as oxidative phosphorylation [22]. ATP drives fundamental biochemical reactions and cell functions through hydrolysis into adenosine diphosphate (ADP) and phosphate anions at the sites where energy is required in cells. In fact, mitochondria have their own circular DNA (mtDNA), which encodes thirteen different protein subunits of enzyme complexes involved in the oxidative phosphorylation process. In addition to their role as energy suppliers, mitochondria are the principal regulators of the apoptotic pathways. Mitochondria dysfunction as a result of damage on mtDNA or mitochondrial membrane depolarization induces an apoptotic response by releasing cytochrome *c* and other apoptosis-related proteins into the cytosol and activates the caspase pathway [23]. Therefore, a rational design of new Ir(III) biscyclometalated cationic complexes, based on a suitable combination of lipophilic and hydrophilic ligands and counteranions, can lead to mitochondria targeted anticancer agents [24,25] and in-depth mechanistic studies can contribute to elucidate their biological mechanism of action.

Previously, we reported on the PDT activity of two Ir(III) complexes of general formula [Ir(C^N)$_2$(N^N′)]Cl (**[Ir1] Cl**, N^N′ = thiabendazole (tbz); or **[Ir2] Cl**, N^N′ = N-benzyl-thiabendazole (Bn-tbz)) and found out that replacement of the reactive N—H group in **[Ir1] Cl** with the N-Bn group in **[Ir2] Cl** prevents deprotonation and leads to higher cellular uptake [26]. Following with our investigations in the field, more recently we have found that a second generation complex of the same type, **[Ir3] Cl**, with a thiabendazole-based N,N′-ligand bearing an alkylacetamide substituent (N-CH_2CONH_2) provides a better excited state lifetime than the analogue complex with the 2-pyridyl-benzimidazole scaffold in the N,N′-ligand [27]. Moreover, it is well-known that the C^N ligands exert a great influence on the photophysical properties of these photosensitizers. In particular, electron-withdrawing groups on the C^N ligands stabilize the HOMO (Highest Occupied Molecular Orbital) provide higher HOMO-LUMO (Lowest Unoccupied Molecular Orbital) energy gaps and usually exhibit longer triplet excited state lifetimes [28,29], which favours the interaction with O_2 to form either $^1O_2$ or $O_2^{\bullet-}$. As a matter of fact, Mao has reported a family of Ir(III) PSs, where the derivative with 2-(2,4-difluorophenyl)pyridinate as the C^N ligand exhibits the highest phototoxicity index (PI = 18.9) upon exposure to blue light [30].

With these premises in mind, we decided to synthesize two sets of new Ir(III) bis-cyclometalated complexes of formula [Ir(C^N)$_2$(N^N′)]Cl, combining two C^N ligands (2-phenylpyridinate (ppy) and 2-(2,4-difluorophenyl)pyridinate (dfppy)) and four different thiabendazole-based N^N′ ligands with diverse alkyl substituents on the N atom (N-R). In particular, we have chosen several alkyl-ketone or alkyl-amide groups which could be used in future derivatizations of these metallodrugs. Hence, the rationale behind the design of these complexes is to achieve new photosensitizers as potential anticancer PDT agents endowed with pH stability, good cellular uptake and long triplet excited state lifetimes to produce ROS. Moreover, we intend to assess the influence of two different structural features on the electrochemical, photophysical and biological properties of these complexes and particularly on their PI: (1) the effect of the different alkyl substituents and (2) the effect of the two afore-mentioned C^N ligands. Besides, we have examined different aspects of their mechanism of biological action, including uptake pathway, organelle localization, cell death, ROS generation, mtDNA damage, etc. As a result, we have established some structure-activity relationships and we have identified two metallodrugs as the most efficient PSs in the potential treatment of cancer. Last but not least, we have outlined the mechanism of biological action upon light excitation for these chemo-therapeutics.

2. Material and methods

2.1. General information

All synthetic manipulations were carried out under an atmosphere of dry, oxygen-free nitrogen using standard Schlenk techniques. The solvents were dried and distilled under nitrogen atmosphere before use. Elemental analyses were performed with a Thermo Fisher Scientific EA Flash 2000 Elemental Microanalyzer. IR spectra were recorded on a Jasco FT/IR-4200 spectrophotometer (4000–400 cm^{-1} range) with Single Reflection ATR Measuring Attachment. UV–Vis absorption was measured in an Evolution 300 UV–Vis double beam spectrophotometer (Thermo Scientific). Fluorescence steady-state and lifetime measurements were performed in a FLS980 (Edinburg Instruments) Fluorimeter with Xenon Arc Lamp 450 W and TCSPC laser, respectively. Quantum Yield was determined by using in a FLS980 (Edinburg Instruments) with Xenon Arc Lamp 450 W and Red PMT Sphere as detector. HR-ESI(+) Mass spectra (position of the peaks in Da) were recorded with an Agilent LC-MS system (1260 Infinity LC/6545 Q-TOF MS spectrometer) using dichloromethane (DCM) /dimethyl sulfoxide (DMSO) (4:1) as the

sample solvent and (0.1%) aqueous HCOOH/methanol as the mobile phase. The experimental *m/z* values are expressed in Da compared with the *m/z* values for monoisotopic fragments. NMR (nuclear magnetic resonance) samples were prepared by dissolving the suitable amount of compound in 0.5 mL of the respective deuterated solvent and the spectra were recorded at 298 K on a Varian Unity Inova-400 (399.94 MHz for ^{1}H; 376.29 MHz for ^{19}F; 100.6 MHz for ^{13}C). Typically, ^{1}H NMR spectra were acquired with 32 scans into 32 k data points over a spectral width of 16 ppm. ^{1}H and ^{13}C{^{1}H} chemical shifts were internally referenced to TMS via the residual ^{1}H and ^{13}C signals of DMSO-d_6 ($\delta = 2.50$ ppm and $\delta = 39.52$ ppm), according to the values reported by Fulmer et al. [31] Chemical shift values (δ) are reported in ppm and coupling constants (J) in Hertz. The splitting of proton resonances in the reported ^{1}H NMR data is defined as s = singlet, d = doublet, t = triplet, q = quartet, m = multiplet, bs = broad singlet. In the ^{1}H NMR resonances, the couplings are H—H, unless otherwise stated. 2D NMR spectra such as ^{1}H—^{1}H gCOSY, ^{1}H—^{1}H NOESY, ^{1}H—^{13}C gHSQC and ^{1}H—^{13}C gHMBC were recorded using standard pulse sequences. The probe temperature (±1 K) was controlled by a standard unit calibrated with methanol as a reference. All NMR data processing was carried out using MestReNova version 10.0.2.

Starting materials. $IrCl_3{\cdot}xH_2O$ was purchased from Johnson Matthey and used as received. The starting dimers ($[Ir_2Cl_2(ppy)_4]$) and ($[Ir_2Cl_2(dfppy)_4]$) (dfppy = 2-(2,4-difluorophenyl)pyridinate)) were prepared according to the reported procedure [32]. The reagents 2-phenylpyridine, 2-(2,4-difluorophenyl)pyridine), (4-thiazolyl)benzimidazole (thiabendazole), benzylamine, aniline and piperidine were purchased from Sigma-Aldrich; 2-bromoacetophenone and bromoacetyl bromide were purchased from Alfa Aesar. All of them were used without further purification. Deuterated solvents (DMSO-d_6) were obtained from Eurisotop. Conventional solvents such as diethyl ether (Fisher Scientific), acetone (Fisher Scientific), 2-ethoxyethanol (Across Organics), 2-methoxyethanol (Across Organics), dimethyl sulfoxide (Scharlau), *N*, *N*-dimethylformamide (Scharlau), ethanol (Scharlau), methanol (Scharlau), dichloromethane (Scharlau), toluene (Across Organics), were degassed and in some cases distilled prior to use. Tetrabutylammonium hexafluorophosphate ($[^{n}Bu_4N][PF_6]$) was purchased from Acros and potassium carbonate from Scharlau.

2.2. Determination of the ability of $^{1}O_2$ generation

The generation of singlet oxygen ($^{1}O_2$) was studied for selected Ir(III) compounds in acetonitrile according to a relative procedure adapted from the literature [33–35], which is based on monitoring by UV–Vis spectroscopy the oxidation of 1,3-diphenylisobenzofuran (DPBF, yellow) to 1,2-dibenzoylbenzene (colorless) photosensitized by the Ir(III) derivatives.

DPBF was selected as the $^{1}O_2$ scavenger due to its fast reaction with $^{1}O_2$. Air-equilibrated acetonitrile solutions containing DPBF were prepared ($\sim 8{\cdot}10^{-5}$ M) in a cuvette and their absorbance adjusted to around 1.0 at 410 nm. Then, the complex (10^{-5} M, corresponding to absorbance around 0.2) was introduced in the cuvette. Low dye concentrations were used to minimize quenching of $^{1}O_2$ by the dyes. The mixture was irradiated with a blue LED strip ($\lambda_{ir} = 460$ nm) at room temperature for 1 s irradiation intervals during a total exposure period of 8 s and absorption UV–Vis spectra were recorded after every irradiation interval.

2.3. Cell lines

Human prostate adenocarcinoma (PC-3) and melanoma (SK-MEL-28) cell lines and CCD-18Co normal fibroblast were purchased from the American Type Culture Collection (ATCC). Cells were maintained in Dulbecco's modified Eagle's medium (DMEM) (Lonza) supplemented with 10% fetal bovine serum (FBS) (Gibco-BRL), 1% L-glutamine (Lonza) and 1% penicillin-streptomycin (Lonza) at 37 °C in a humidified atmosphere containing 5% CO_2. Cells were maintained by successive trypsinization and seeding. Possible contamination with Mycoplasma was routinely checked using the VenorH GeM Mycoplasma Dection Kit (Minerva Biolabs).

2.4. Photoactivation protocol

For photodynamic studies, cells were preincubated with the compounds for 1 h or 6 h, to allow their cellular uptake. Then, cells were irradiated at 460 nm for 1 h with a LED system (LuxLight) capable of illuminating the whole culture plate with an effective power of 6.7 mW cm^{-2}, giving a dose of 24.1 J cm^{-2}.

2.5. Cytotoxicity experiments

To assess the cytotoxic activity of the compounds, PC-3, SK-MEL-28 or CCD-Co18 cells were seeded onto flat-bottomed 96-well plates at a density of 4000, 2500 and 6000 cells per well respectively, 24 h prior to the treatments. Compounds were diluted in sterile milli-Q water and DMSO to prepare 1 mM stock solutions that were diluted in culture medium to obtain concentrations ranging from 0 to 50 μM. The final concentration of DMSO in these solutions did not exceed 1%. Cells were treated with the solutions in the dark or following the photoactivation protocol. After 48 h of treatment (including the preincubation and irradiation times) cell viability was determined by the 3-(4,5-dimethylthiazol-2-yl)-2,5-diphenyltetrazolium bromide (MTT) assay as previously described. Four replicates for each treatment were used and all treatments were tested in three independent experiments. The concentration that reduces the cell viability by 50% (IC_{50}) was established for each compound using the Gen5 software (BioTek). Compounds with IC_{50} values greater than 50 μM were considered to be inactive. The phototoxicity index (PI = $IC_{50,dark}/IC_{50,light}$) of the compounds was determined.

2.6. Hemolytic assay

The hemolytic activity of the compounds at concentrations from 0 to 50 μM was evaluated by determining hemoglobin release from erythrocyte suspensions of fresh porcine blood (5% vol/vol). Triton X-100 0.2% in phosphate buffer saline (PBS) was used as positive control. 150 μLof diluted erythrocytes were mixed with 150 μL of the compound solutions and incubated at 37 °C for 1 h in an orbital shaker. Samples were centrifuged to pellet intact erythrocytes and 80 μL of supernatant was transferred to a 96-well plate and diluted with 80 μL of H_2O. The absorbance of each well was measure with a Synergy 4 plate reader (Biotek) at 540 nm. The percentage of hemolysis was obtained from the ratio between the absorbance of each sample and the absorbance of the positive control. Each concentration was assayed in triplicate.

2.7. Colony formation assay

PC-3 cells were seeded in 24-well plates. 24 h later, cells were preincubated for 6 h with **[1a]Cl** or **[3a]Cl** at the corresponding $IC_{50,light}$ and then kept in the dark or photoactivated for 1 h. Cells were exposed to cisplatin (50 μM) or vehicle alone as a control for the same period of time. Then, cells were washed with PBS, collected by trypsinization and plated at low density (3000 cells in a 35-mm cell culture dish). Cells were allowed to divide and form colonies for 10–14 days; after which, colonies were fixed and stained with 2% methylene blue in 50% ethanol. The number of colonies (of 50 cells or more) in each plate was determined using the Alpha Innotech Imaging system (Alpha Innotech, San Leandro, CA) and the Fiji ImageJ software.

2.8. Cell internalization experiments

The uptake of the compounds in PC-3 cells was quantified by flow cytometry. For internalization kinetics studies, 100,000 cells were

seeded in 24-well plates. 24 h later, cells were incubated with the compounds at 5 μM or medium alone as a control for 1, 4, 6 and 16 h at 37 °C. Then, cells were washed with cold PBS and harvested by trypsinization. Next, 10,000 cells were analysed with a Novocyte flow cytometer (Agilent Technologies) equipped with the NovoExpress® software. The fluorescence of **[1a]Cl** and **[3a]Cl** was detected in the FL-1 channel (excitation at 488 nm; emission at 530 nm). At the different time points, the percentage of cells with positive green fluorescence was determined relative to untreated control cells and the measured data were fitted to one-phase exponential association curves with GraphPad Prism software (GraphPad Software, Inc., USA) [36].

The cellular uptake mechanism was investigated by inhibition of different internalization pathways followed by the determination of the intracellular levels of the compounds. As positive control, cells were incubated with the compounds dissolved in DMEM (without FBS) at 5 μM for 1 h at 37 °C. To inhibit pathways that require metabolic energy, cells were incubated at 4 °C for 1 h. To specifically inhibit endocytosis, cells were first incubated for 30 min at 37 °C with dynasore (Focus Biomolecules) dissolved at 100 μM in DMEM and then incubated at 37 °C with the compound solutions for one additional hour. Next, cells were washed with PBS and detached with trypsin. The intracellular fluorescence of 10,000 cells was analysed by flow cytometry as described above.

2.9. Confocal microscopy

Cellular localization of the compounds was assessed by confocal fluorescence microscopy. SK-MEL-28 cells were selected for these experiments since they displayed a strong mitochondrial staining. 100,000 cells were seeded on coverslips and allowed to attach overnight. Next, cells were treated with **[1a]Cl** or **[3a]Cl** diluted at 25 μM in DMEM without FBS or with medium alone as control. Colocalization with mitochondria was analysed with the mitochondria-specific dye MitoTracker™ Red CMXRos (Molecular Probes) at a 100 nM final concentration. Cells were incubated for 1 h at 37 °*C*. Medium was removed and cells were washed with cold PBS and fixed with 4% paraformaldehyde in PBS for 15 min at 4 °C. After washing twice with PBS, the coverslips were mounted using ProLong™ Antifade Mountant (Invitrogen). Images were taken on a Nikon A1R confocal microscope and analysed using the NIS-Elements AR (Nikon, Japan) and Fiji ImageJ software. The JACoP plugin was used to calculate the Pearson's coefficient (to measure the linear relationship between the signal intensities) and Mander's M1 and M2 overlap coefficients (to measure the colocalization coefficient between the fluorophores) [37].

2.10. Electrophoretic mobility experiments

The effect of the complexes on DNA was analysed using the pUC18 plasmid DNA (ThermoScientific). Treatments were carried out mixing 250 ng of pUC18 (stock solution at 0.5 μg/μL, final concentration at 37.8 μM in nucleotides) and compounds solutions at up to 100 μM (final volume of 20 μL). The treatments were freshly prepared in saline-TE (50 mM NaCl, 10 mM tris(hydroxymethyl) aminomethane−HCl, 0.1 mM ethylenediaminetetracetic acid (EDTA), pH 7.4) from a 1 mM solution of the complex in 20% DMSO, giving a final DMSO concentration in the treatments of less than 2% . Samples were incubated at room temperature for 1 h, either protected from light or under irradiation (6.7 mW cm^{-2}, total dose of 24.1 J cm^{-2}). Reactions were quenched by adding a loading buffer solution (4 μL) consisting of bromo-phenol blue (0.25%), xylenecyanole (0.25%), and glycerol (30%). The samples were then subjected to electrophoresis on 0.8% agarose gel in 0.5× TBE buffer (0.045 M Tris, 0.045 M boric acid, and 1 mM EDTA) at 100 V for 1 h 40 min. Finally, the DNA was dyed with an ethidium bromide solution (0.5 μg/mL in 0.5× TBE buffer) for 30 min and the DNA bands were visualized on a capturing system (ProgRes CapturePro 2.7). Images were cropped and inverted to better appreciate plasmid bands using Adobe Photoshop. Densiometric analyses of the bands were carried out using the Fiji ImageJ Software.

To detect ROS generation during the treatment, various ROS scavengers were added to the reaction mixtures: 15% DMSO (hydroxyl radical scavenger), 0.4 M sodium azide (oxygen singlet scavenger) and 10 mM tiron (4,5-dihydroxy-1,3-benzenedisulfonic acid) (superoxide anion scavenger). Sodium azide and tiron 10 mM solutions were prepared in saline-TE buffer. A treatment with 1.75% H_2O_2 and 20 μM $FeCl_2$ was used a positive control of ROS generation and nuclease activity on DNA. Samples were then treated as explained above. Experiments were conducted in triplicates.

2.11. RT-qPCR and gene expression analysis

PC-3 cells were incubated with **[1a]Cl** or **[3a]Cl** at the corresponding $IC_{50,light}$ under photoactivated conditions (with 6 h of preincubation) or medium alone as a control. After 24 h, the cells were harvested by trypsinization and total RNA was extracted using TRIzol Reagent (Invitrogen) according to the manufacturer's protocol. The concentration and quality of the extracted RNA was determined by a PowerWave XS2 Spectrophotomer (Bio-Tek Instruments), measuring the absorbance at 260 nm and calculating the ratio of absorbances at 260 and 280 nm, respectively. RNA (2.5 μg) was converted into cDNA using M-MLV Reverse Transcriptase (Invitrogen) and a mixture of 250 ng of random hexamer primers (EURx) and 250 ng of oligo $(dT)_{20}$ primers (EURx), according to the manufacturer's manual. RT-qPCR was carried on a fluorometric thermal cycler iCycler IQTM Real-time Detection System (Bio-Rad). Specific primers (Table SI-1) were designed using NCBI tool Primer-BLAST (https://www.ncbi.nlm.nih.gov/tools/primer-blast/). One qPCR reaction (25 μL) contained 1× SYBR-Green Master Mix (EURx), 480 nM of each primer and 5 μL of cDNA (ten-fold dilution). The PCR profile was: 3 min at 95 °C, followed by 40 cycles of 30 s at 95 °C and 1 min at 59 °C (COX1 system) or 62 °C (ND3 and ACTB system). Four RT-qPCR analysis were conducted with each of two independent biological replicates.

Relative mRNA expression levels of the mitochondrial genes *NADH dehydrogenase subunit 3* (*ND3*) and *cytochrome c oxidase* subunit I *(COX1)* were calculated by the ratio (Efficiency of target gen)$^{\Delta Cq,target(control-sample)}$/ (Efficiency of reference gen)$^{\Delta Cq,reference(control-sample)}$ [38], with *β-actin* (*ACTB*) as a reference gene [39]. The PCR amplification efficiency was determined by running standard curves for each system in different template dilutions (Table SI-2).

2.12. Evaluation of mitochondrial membrane potential

The effect on the mitochondrial membrane potential was measured by the JC-1 (5,5′,6,6′-tetrachloro-1,1′,3,3′-tetraethylbenzimidazolylcarbocyanine iodide) dye. 100,000 PC-3 cells were seeded in 24-well plates. 24 h later, cells were exposed for 6 h to **[1a]Cl** or **[3a]Cl** at the corresponding $IC_{50,light}$ followed by 1 h of photoactivation or incubation in dark conditions. Next, cells were washed with PBS and harvested by trypsinization. Mitochondrial membrane potential changes were measured with the JC-1 Mitochondrial Membrane Potential Detection Kit (Biotium), according to the manufacturer's instructions. For positive control, cells were coincubated with carbonyl cyanide 3-chlorophenylhydrazone (CCCP) at 50 μM. Samples were immediately analysed by a Novocyte flow cytometer. Healthy mitochondria containing red JC-1 aggregates were detected at an emission wavelength of 590 nm (FL2) and green JC-1 monomers in cells with depolarized mitochondria were monitored at 529 nm (FL1).

2.13. Superoxide radical detection

Superoxide radical levels in PC-3 cells were measured using the ROS-ID Superoxide detection kit (Enzo-Life Sciences) according to the supplier's instructions. Briefly, 100,000 cells per well were seeded in a 24-

well plate and allowed to attach for 24 h. Cells were preincubated for 6 h with **[1a] Cl** and **[3a] Cl** at the corresponding $IC_{50,light}$ and then kept in the dark or photoactivated for 1 h. Cells exposed to the ROS inducer pyocyanin at 250 μM for 30 min were used as positive control. Untreated cells were used as negative control. Cells were harvested by trypsinization, washed and incubated in the dark for 30 min in buffer containing the fluorescent probe. Samples were immediately analysed by a Novocyte flow cytometer. Cells with increased production of superoxide were detected by higher orange fluorescence in the FL2 channel (Ex/Em: 550/620 nm).

2.14. Annexin V-FITC/propidium iodide apoptosis analysis

Analysis of phosphatidylserine externalization in apoptotic cells was determined by a Vybrant® Apoptosis Assay Kit (Molecular Probes), according to the manufacturer's instructions. 100,000 PC-3 cells per well were seeded in 24-well plates and incubated with cisplatin at 50 μM or with **[1a] Cl** or **[3a] Cl** at the corresponding $IC_{50,light}$ under photoactivation conditions (with 6 h of preincubation). 24 h later, cells were collected by trypsinization and resuspended in 100 μL of Annexin V-binding buffer with 5 μL of Annexin-V-FITC and 10 μL of propidium iodide. After 15 min of incubation at room temperature, the fluorescence of 10,000 cells was analysed by a NovoCyte flow cytometer using FL1 channel for Annexin-V-FITC and FL2 channel for propidium iodide detection.

2.15. Statistics

The statistical analysis was performed with the GraphPad Prism software. Quantitative variables were expressed as mean or median and standard deviation (SD). Statistical differences were analysed by the Mann-Whitney non-parametric test. A value of $p < 0.05$ was considered significant.

3. Results and discussion

3.1. Synthesis of ligands and iridium(III) complexes

A new library of Ir(III) biscyclometalated compounds of general formula *rac*-[Ir(C^N)$_2$(N^N′)]Cl has been prepared aiming to study their anticancer properties as potential PDT agents. In particular, we have used two different C^N ligands and four different N^N′ ligands based on the 2-(4-thiazolyl)benzimidazole (thiabendazole) scaffold. Thiabendazole (**L0**) is an antifungal and antiparasitic agent commercially available and can be easily functionalized by mean of alkylation reactions on the reactive N—H group. Thus, the ligands (**L1-L4**) with different amido-alkyl and keto-alkyl groups were obtained through a procedure adapted from the literature [40,41], which involves the reaction of **L0** with the appropriate alkyl bromide at room temperature in the presence of K_2CO_3 and using dimethylformamide (DMF) as solvent (Scheme 1). Ligands **L1-L4** were designed to possess protecting hydrophilic motifs instead of the slightly acidic N—H on the imidazole ring, such as hydrogen bonding donor and acceptor groups, which can bestow a certain degree of hydrophilicity on the resulting complexes by contrast with the lipophilicity attributed to the $[Ir(C^N)_2]^+$ fragment.

The corresponding Ir(III) derivatives **[1a] Cl** – **[4a] Cl** (series A) and **[1b] Cl** - **[4b] Cl** (series B) were synthesized by refluxing the appropriate iridium dimer $[Ir(\mu\text{-}Cl)(C^N)_2]_2$ (C^N = ppy (2-phenylpyridinate), or dfppy (2-(2,4-difluorophenylpyridinate)) in the presence of ligands **L1-L4** in a mixture of dichloromethane-methanol (1:1.25; *v*/v) (Scheme 1). The desired products were isolated as solid chloride salts in the form of racemic mixtures with bright yellow colours and display moderate solubility in aqueous media because of the presence of hydrophilic groups and the chloride counterion.

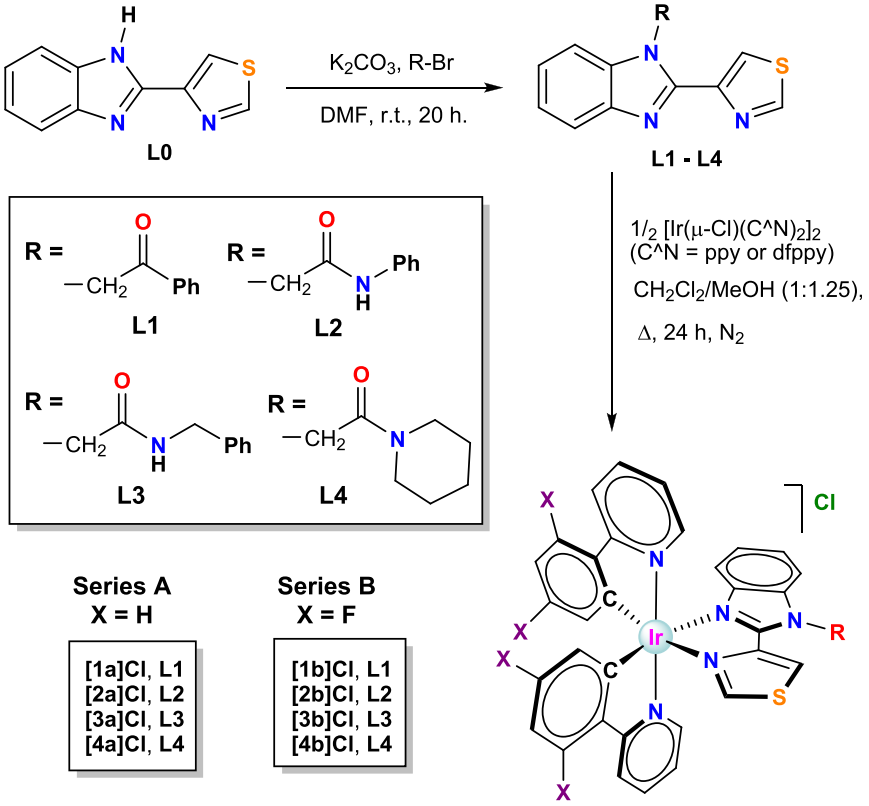

Scheme 1. Synthesis and molecular structures of ligands **L1** – **L4** and complexes **[1a] Cl** - **[4a] Cl** and **[1b] Cl** - **[4b] Cl**.

3.2. Characterization of the Ir(III)-compounds

The composition and molecular structure of the new Ir complexes was established by multinuclear NMR, mass spectrometry, elemental analysis and IR spectroscopy. In addition, the molecular structure of complexes **[1b]**$^{+}$, **[2a]**$^{+}$ and **[3a]**$^{+}$ was ascertained by X-ray diffraction.

The ^{1}H, ^{13}C{^{1}H} and ^{19}F NMR spectra of **[1a] Cl** - **[4a] Cl** and **[1b] Cl** - **[4b] Cl** were recorded in DMSO-d_6 (Figure SI12-SI31) and show evident coordination-induced shifts relative to the free ligands and the

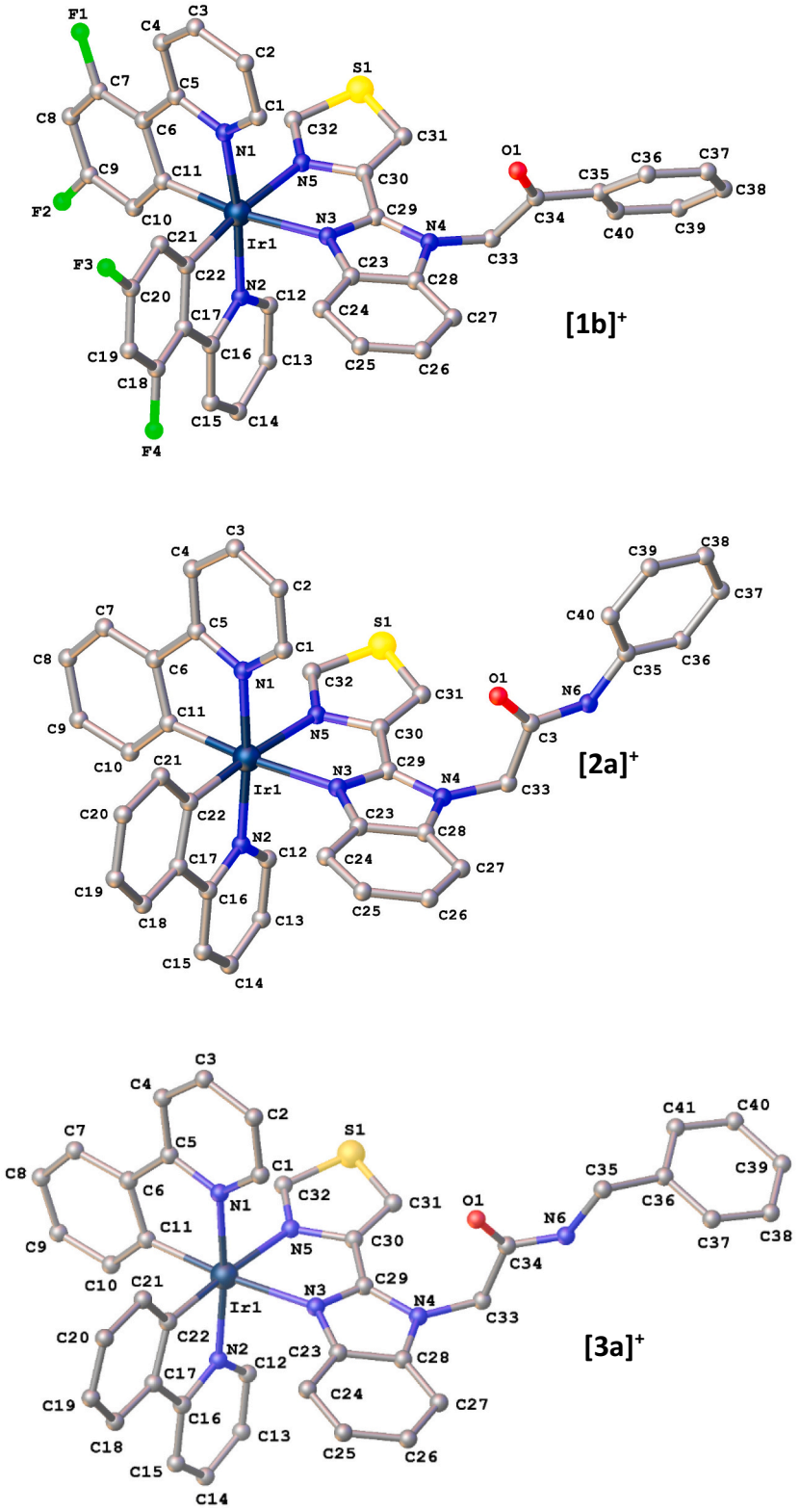

Fig. 1. Molecular structures of (Λ)-**[1b] PF_6**, (Λ)-**[2a] PF_6** and (Λ)-**[3a] PF_6** obtained by X-ray diffraction analysis. The Δ enantiomers, H atoms and PF_6^- counterions have been omitted for the sake of clarity.

following distinguishing attributes: (1) two sets of signals for the non-equivalent CˆN ligands (C_1-symmetry); (2) two mutually coupled doublets, appearing as an AB quartet between 5.65 and 6.75 ppm for the diastereotopic protons of the $–CH_2$ groups because of the helical chirality implicit in tris-chelate octahedral complexes.

The ^{19}F NMR spectra of complexes **[1b] Cl** - **[4b] Cl** display two multiplets around −107 ppm (F^9 and $F^{9'}$) and two additional multiplets at about −109 ppm (F^{11} and $F^{11'}$), for the two non-equivalent dfppy (atom labelling shown in ESI).

The HR ESI(+) mass spectra of **[1a] Cl** - **[4a] Cl** and **[1b] Cl** - **[4b] Cl** show an envelope of peaks with *m/z* values and isotopic distribution patterns fully compatible with those calculated for the monocationic species of formula $[Ir(C^N)_2(N^N')]^+$, resulting from the loss of the chloride counterion in every case (ESI).

3.3. Crystal structures by X-ray diffraction

High quality single crystals were obtained for the PF_6^- salts of **[1b]**$^+$, **[2a]**$^+$ and **[3a]**$^+$ by slow evaporation of solutions of either **[1b] Cl** and **[3a] Cl** in methanol or **[2a] Cl** in methanol/dichloromethane, upon addition of some drops of saturated aqueous NH_4PF_6 in order to facilitate crystallization. The corresponding crystal structures of **[1b] PF_6**, **[2a] PF_6** and **[3a] PF_6** were resolved by single crystal X-ray diffraction analysis. The complexes crystallize in the monoclinic $P2_1/c$, C2/c and C2/c space groups, respectively. The unit cells of these complexes contain two pairs (**[1b] PF_6**) or four pairs (**[2a] PF_6** and **[3a] PF_6**) of enantiomers (Δ,Λ) plus four or eight PF_6^- counteranions. The molecular structures for the Λ enantiomers of complex cations **[1b]**$^+$, **[2a]**$^+$ and **[3a]**$^+$ are shown in Fig. 1. Selected bond distances and angles for the coordination environment are compiled in Table 1, and relevant crystallographic parameters are given in Table SI-3.

The molecular structures of these complexes exhibit the expected pseudo-octahedral geometry around the Ir centre with two cyclometalating CˆN ligands adopting a mutual *trans*-N,N plus *cis*-C,C arrangement. Besides, each NˆN′ ligand assumes a *trans* disposition with regard to the C atoms of the CˆN moieties (Fig. 1) [42]. As an evidence of deviation from the ideal octahedral geometry, all the bite angles for the bidentate ligands are lower than 90°, i.e. around 80° for the CˆN ligands, and about 76° for the NˆN′ ligands (Table 1). In all the complexes, the Ir—N bond distances for the CˆN ligands (2.039(5) to 2.047(5) Å) are shorter than for the NˆN′ ligands (2.157(5) to 2.165(4) Å) due to the strong *trans* influence exerted by the coordinated phenyl rings [43]. The Ir—C bond distances are very close to 2 Å (2.003(6)-2.016(6) Å) and

Table 1
Selected bond lengths (Å) and angles (°) for **[1b] PF_6**, **[2a] PF_6** and **[3a] PF_6**.

[1b] PF_6		**[2a] PF_6**		**[3a] PF_6**	
Ir(1)-N(1)	2.038 (6)	Ir(1)-N(1)	2.047 (5)	Ir(1)-N(1)	2.041(4)
Ir(1)-N(2)	2.050 (6)	Ir(1)-N(2)	2.039 (5)	Ir(1)-N(2)	2.049(4)
Ir(1)-N(3)	2.151 (6)	Ir(1)-N(3)	2.165 (4)	Ir(1)-N(3)	2.171(4)
Ir(1)-N(5)	2.155 (5)	Ir(1)-N(5)	2.157 (5)	Ir(1)-N(5)	2.159(4)
Ir(1)-C(11)	2.009 (7)	Ir(1)-C(11)	2.016 (6)	Ir(1)-C(11)	2.016(5)
Ir(1)-C(22)	2.013 (7)	Ir(1)-C(22)	2.003 (6)	Ir(1)-C(22)	2.004(5)
C(11)Ir(1)N (1)	81.3(3)	C(11)Ir(1)N (1)	81.4(2)	C(11)Ir(1)N (1)	81.12 (19)
C(22)Ir(1)N (2)	79.5(3)	C(22)Ir(1)N (2)	81.3(2)	C(22)Ir(1)N (2)	80.72 (18)
N(3)Ir(1)N (5)	76.1(2)	N(3)Ir(1)N (5)	75.6(2)	N(3)Ir(1)N (5)	75.31 (14)

The 3-*D* crystal structures of these complexes are stabilized by hydrogen bonding interactions, involving C—H and N—H groups as donors and C═O groups as well as PF_6^- anions as acceptors.

standard compared to those usually observed for similar complexes [44].

3.4. Photostability experiments

Photostability under long irradiation is a key requirement for PDT photosensitizers, since it ensures more ROS-producing cycles for the PS and allows to reduce the PS dose [45]. In other words, a high photostability favours the PS efficiency. The photodegradation of the new Ir (III)-complexes was analysed by monitoring the changes in their ^1H NMR spectra ($1.4{\cdot}10^{-2}$ M, CD_3CN) over a period of 24 h under air exposure and illumination with blue light, ($\lambda_{ir} = 460$ nm, 24 W) at room temperature (Figure SI-33 to SI-40). All the complexes are fully stable upon 6 h of irradiation, since no photo-degradation was observed during this period. However, after 24 h of irradiation we detected an emerging set of signals for degradation products that integrated between 1% and 5% (Table SI-4). These results confirm the sufficient photostability of our luminophores for PDT applications.

3.5. Theoretical calculations

Density functional theory (DFT) and time-dependent DFT (TD-DFT) calculations were carried out on the molecular and electronic structures of the cation complexes **[1a]**$^+$, **[3a]**$^+$, **[1b]**$^+$ and **[3b]**$^+$ at their ground state for a deeper comprehension of their photophysical and electrochemical properties. Calculations were performed at the B3LYP/(6-31GDP + LANL2DZ) level including solvent effects (CH_3CN) (see description in ESI and Tables SI-3, SI-4 and SI-5). The optimized molecular structures calculated for **[1a]**$^+$, **[3a]**$^+$, **[1b]**$^+$ and **[3b]**$^+$ at their electronic ground state (S_0) exhibit a near-octahedral geometry for the metal coordination environment in agreement with the crystal structures previously discussed. Table SI-5 shows the isovalue contour plots and the energies for the frontier molecular orbitals (MOs) of cations **[1a]**$^+$, **[3a]**$^+$, **[1b]**$^+$ and **[3b]**$^+$ at the S_0 state. The HOMOs of these complexes are spread over the Ir and the phenyl or difluorophenyl rings of the CˆN ligands and are formed by an admixture of a t_{2g} orbital from Ir(III) and π orbitals of the two phenyl rings. Consequently, the energies computed for the HOMOs of **[1a]**$^+$ and **[3a]**$^+$ are virtually identical (−5.61 and − 5.62 eV), given that they have the same CˆN ligands (ppy^-). Similarly, the energies obtained for the HOMOs of **[1b]**$^+$ and **[3b]**$^+$ are almost alike (−5.94 and − 5.95 eV), since they share the same CˆN ligands ($dfppy^-$). The stabilization of the HOMOs for **[1b]**$^+$ and **[3b]**$^+$, relative to the HOMOs of **[1a]**$^+$ and **[3a]**$^+$ is due to the electron-withdrawing nature of the -F atoms in $dfppy^-$, as reported previously (Fig. 2) [46,47].

The LUMOs are distributed over the NˆN′ ligands in all the cases, although their precise topology depends slightly on the ligand. Indeed, the participation of the alkyl group of **[1a]**$^+$ and **[1b]**$^+$ ($-CH_2COPh$) in the electron density of their LUMO is relevant, while the participation of the alkyl group of **[3a]**$^+$ and **[3b]**$^+$ ($-CH_2CONHCH_2Ph$) in their LUMO is non-existent. The LUMO of **[3a]**$^+$ exhibits a small destabilization relative to that of **[1a]**$^+$ and a similar effect was observed for **[3b]**$^+$ compared to **[1b]**$^+$. These predictions are in agreement with the electrochemical trends experimentally determined for the reduction potentials of these complexes (see below). Considering all the above, the resulting HOMO-LUMO gaps are higher for complexes of series B than for their congeners of series A.

The nature of the lowest-energy singlet (S_n) and triplet (T_n) excited states and the respective energies were computed by mean of the TD-DFT method for the cations **[1a]**$^+$, **[3a]**$^+$, **[1b]**$^+$ and **[3b]**$^+$. The results are compiled in Tables SI-6 and SI-7 and are sketched in Fig. SI-41 (a). The lowest triplet excited states (T_1) of **[1a]**$^+$ and **[3a]**$^+$ exhibit energies of 2.75 eV, while the corresponding states of **[1b]**$^+$ and **[3b]**$^+$ are destabilized to 2.85 eV. Hence, these estimations predict lower λ_{em} for **[1b]**$^+$ and **[3b]**$^+$ relative to **[1a]**$^+$ and **[3a]**$^+$ in agreement with the trends determined experimentally for the emission energies of these

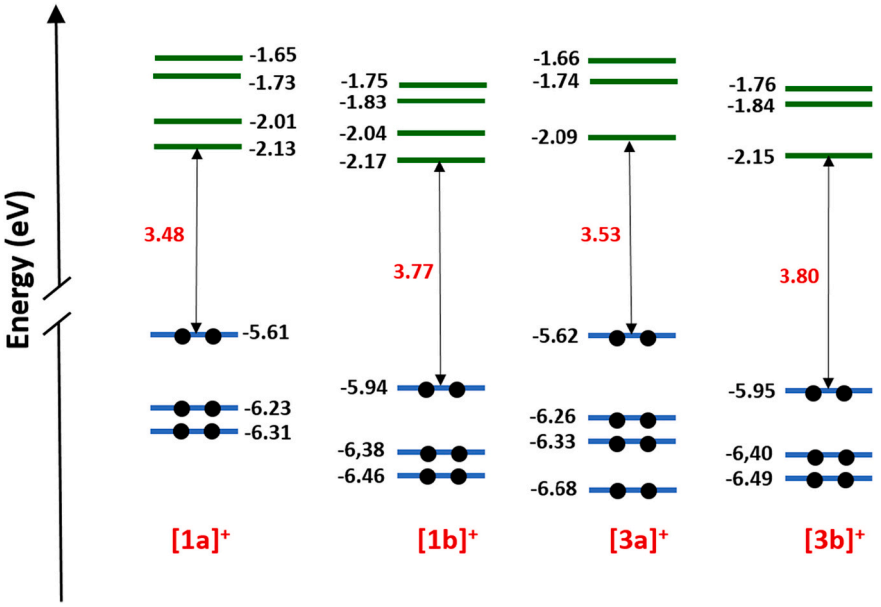

Fig. 2. Schematic representation displaying the energies computed for the frontier orbitals and the HOMO-LUMO energy gaps of **[1a]** $^{+}$, **[3a]** $^{+}$, **[1b]** $^{+}$ and **[3b]** $^{+}$.

pairs (see below).

3.6. Electrochemical properties

The electrochemical behaviour of the ground and excited states of this type of complexes can play important roles in their biological activity both in the dark and upon photoactivation, respectively [48]. For that reason, the redox potentials of **[1a] Cl** - **[4a] Cl** and **[1b] Cl** - **[4b] Cl** were experimentally determined by cyclic voltammetry (CV) in deoxygenated acetonitrile solutions (5×10^{-4} M) versus the ferrocenium/ferrocene (Fc^{+}/Fc) couple. The cyclic voltammograms of **[1a] Cl** - **[1b] Cl** and **[3a] Cl** - **[3b] Cl** are shown in Fig. 3(A) as illustrative examples of their respective series. Voltammograms for the other derivatives are very similar to those of **[3a] Cl** and **[3b] Cl** and are presented in the ESI (Figure SI-42-SI-44).

The anodic region of the voltammograms features one irreversible peak for all the complexes between +0.56 and + 0.69 V ($E^{ox1}{}_{1/2}$ in Table 2 and Fig. 3(A)) attributed to the oxidation of the Cl^{-} counter-anion ($2\ Cl^{-} \rightarrow Cl_2 + 2\ e^{-}$). This assignation was confirmed by recording the CV of **[3a] PF_6**, where the afore-mentioned peak was

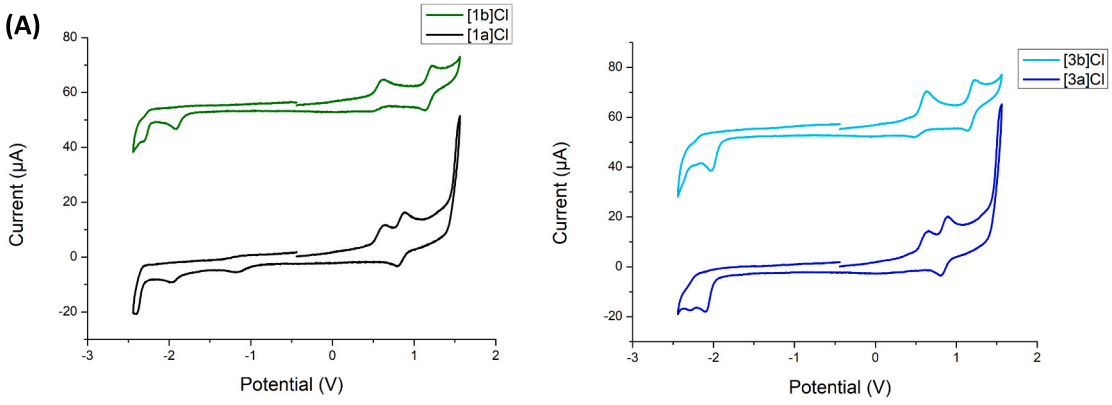

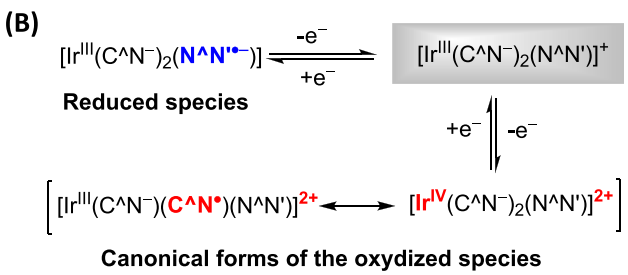

Fig. 3. (A) Cyclic voltammograms of complexes **[1a] Cl** - **[1b] Cl** and **[3a] Cl** - **[3b] Cl** in acetonitrile solution (5×10^{-4} M), using 0.1 M [nBu$_4$N][PF_6] as supporting electrolyte and recorded with a scan rate of 0.10 V·s^{-1}. (B) Reduced and oxidized species formed for complexes of formula $[Ir^{III}(C\hat{}N^{-})_2(N\hat{}N')]^{+}$.

Table 2
Redox potentials recorded by cyclic voltammetry referenced to Fc^+/Fc in acetonitrile solution.[a,b]

Complex	$E^{ox1}{}_{1/2}$(V)	$E^{ox2}{}_{1/2}$(V)	$E^{red1}{}_{1/2}$(V)	$E^{red2}{}_{1/2}$(V)	$\Delta E_{1/2}$(V)
[1] (PF_6)	–	+0.87 (rev)	−1.78 (qr)	–	2.65
[1a] Cl	+0.57 (ir)	+0.85 (rev)	−1.96 (ir)	−2.29 (ir)	2.81
[2a] Cl	+0.67 (ir)	+0.85 (rev)	−2.10 (ir)	−2.27 (ir)	2.95
[3a] Cl	+0.65 (ir)	+0.85 (rev)	−2.11 (ir)	−2.26 (ir)	2.96
[4a] Cl	+0.69 (ir)	+0.84 (rev)	−2.04 (ir)	−2.12 (ir)	2.88
[1b] Cl	+0.56 (ir)	+1.18 (rev)	−1.92 (ir)	−2.26 (ir)	3.10
[2b] Cl	+0.67 (ir)	+1.18 (rev)	−2.05 (ir)	−2.20 (ir)	3.23
[3b] Cl	+0.56 (ir)	+1.18 (rev)	−2.03 (ir)	−2.19 (ir)	3.21
[4b] Cl	+0.56 (ir)	+1.17 (rev)	−1.90 (ir)	−2.11 (ir)	3.07
[3a] PF_6	–	+0.85 (rev)	−2.11 (ir)	−2.25 (ir)	2.96

[a] Voltammograms recorded in acetonitrile solution (5×10^{-4} M), using 0.1 M [nBu$_4$N][PF_6] as supporting electrolyte and recorded with scan rate of 0.10 $V{\cdot}s^{-1}$ and referenced to Fc^+/Fc.

[b] Redox potentials for the reference complex have been obtained from the literature [53].

missing (Fig. SI-44). The small variations noticed in the position of this oxidation peak depending on the complex are likely due to weak interactions between chloride and the respective complex cation, which are responsible for the formation of ion pairs (see Molar conductivity measurements below). Moreover, a second reversible one-electron redox peak is observed at +0.85 V for **[1a] Cl** - **[4a] Cl** and at around +1.18 V for **[1b] Cl** - **[4b] Cl**. This wave is assigned to the reversible oxidation of the environment formed by the Ir(III) centre and both phenyl rings of the respective CˆN ligands, in agreement with the topology calculated for the HOMO of **[1a]**$^+$, **[3a]**$^+$, **[1b]**$^+$ and **[3b]**$^+$ (see Table SI-6 and canonical forms in Fig. 3(B)) [49,50]. Thus, this peak is shifted to more anodic potentials (0.33 V, approximately) for complexes of series B, due to the presence of -F atoms on the phenyl rings. The electron-withdrawing effect of the -F atoms reduces the electron density at the Ir-Ph environment and stabilizes remarkably the HOMO (see calculations), hindering the extraction of the first electron from **[1b] Cl** - **[4b] Cl** relative to **[1a] Cl** - **[4a] Cl** [51,52].

The cathodic region, on the other side, displays one irreversible wave peaking at around −2 V for complexes of both series ($E^{red1}{}_{1/2}$ in Table 2). The extra electron accepted by these complexes is accommodated in the NˆN′ ligand [54], in agreement with the topology of their LUMO (see Table SI-5), giving place to a reduced radical form, [Ir^{III}(CˆN$^-$)$_2$(NˆN′$^{\bullet -}$)] (Fig. 3(B)). All the complexes with alkyl-amide groups, except **[4b] Cl**, that is **[2a] Cl** - **[4a] Cl** and **[2b] Cl** - **[3b] Cl**, present more negative reduction potentials $E^{red1}{}_{1/2}$ (in the range from −2.03 to −2.11 V) than the respective complexes with the alkyl-ketone group, namely, **[1a] Cl** and **[1b] Cl** (−1.96 and − 1.92 V, respectively). This effect is likely due to the destabilization of the LUMO predicted theoretically for **[3a]**$^+$ and **[3b]**$^+$ relative to the LUMO of **[1a]**$^+$ and **[1b]**$^+$, and it is attributed to both the positive mesomeric (electron donating) effect of the -CH_2CONR_2 groups and the negative mesomeric (electron withdrawing) effect of the -CH_2COPh group. Moreover, calculations reported by us in a previous work for the reduced species of a similar complex [55], predict a high spin density localized on one of the C atoms of the thiazole ring when the NˆN′ ligand is based on the thiabendazole scaffold. Thus, the irreversible nature of the reduction process observed for our complexes could be rationalized due to the limited delocalization of the afore-mentioned unpaired electron.

The electro-chemical band-gaps ($\Delta E_{1/2}$) have been determined as the difference between $E^{ox2}{}_{½}$ and $E^{red1}{}_{½}$. The so-calculated values are in the range between 2.81 and 2.96 eV for members of family A and in the range between 3.07 and 3.23 for their congeners of family B, which is in accordance with the higher HOMO-LUMO band-gap calculated theoretically for family B. Hence, the afore-mentioned stabilization of the HOMO in family B seems to be the main factor explaining the increase of $\Delta E_{1/2}$ for **[1b] Cl** - **[4b] Cl** relative to **[1a] Cl** - **[4a] Cl**.

Interestingly, the excited states of this type of complexes usually exhibit an outstanding combination of reductive and oxidative character. In particular, our photosensitizers show higher excited state oxidation powers than the archetypal photosensitizer [Ir(ppy)$_2$(bpy)]PF_6, **[1] PF_6**, that is, $E_{1/2}(Ir^{III}*/Ir^{II})$ ranges from +0.47 to +0.83 V relative to +0.28 V for **[1] PF_6**. At the same time, these photosensitizers show better excited state reduction power than **[1] PF_6**, since $E_{1/2}(Ir^{IV}/Ir^{III}*)$ ranges from −1.47 to −1.75 V relative to −1.19 V for **[1] PF_6** (Fig. 4 and Table SI-8). These redox properties *a priori* render our complexes excellent photoredox catalysts, which in turn could enhance their ability to generate ROS and improve their biological performance as PDT agents.

Molar conductivity measurements (Λ_M) were performed for **[3a] Cl** and **[3a] PF_6** in acetonitrile solutions (10^{-3} M) at room temperature. Interestingly, the value obtained for **[3a] PF_6** ($\Lambda_M = 178\ S{\cdot}cm^2{\cdot}mol^{-1}$) is compatible with a 1:1 electrolyte, whereas the value determined for **[3a] Cl** ($\Lambda_M = 81\ S{\cdot}cm^2{\cdot}mol^{-1}$) is remarkably lower revealing the formation of intimate ion pairs for **[3a] Cl** in this solvent. Thus, we hypothesize that the participation of the Cl^- counteranion in ion pairing and the strength of the specific interactions involved in the formation of these entities could explain the small variations observed for $E^{ox1}{}_{1/2}$.

3.7. Photophysical properties

The UV–Vis absorption and emission spectra of the new complexes were recorded in H_2O-DMSO (94:6, v:v) (10^{-5} M) at room temperature (Figs. 5(A) and SI32(A) and Table 3). All the derivatives exhibit strong bands with maxima around 250 nm (^{1}LC, π → π* for CˆN and NˆN′ ligands) and 300 nm (^{1}MLCT and ^{1}LLCT) and a weak but very broad tail above 350 nm (^{3}MLCT and ^{3}LC) [56–58]. This spin-forbidden band is enabled by the large spin-orbit coupling typical of the Ir(III) ion [47] and spreads well into the visible region for **[1a] Cl** - **[4a] Cl**, but faintly for **[1b] Cl** - **[4b] Cl**. The value of ε [$M^{-1}\ cm^{-1}$] at the wavelength used in biological experiments (460 nm) is reflected in Table 3. Indeed, the absorption of derivatives of series A overlaps suitably with the emission band of our blue light source. However, *a priori* the analogues of series B with dfppy can hardly be excited with this light source, which could be a handicap for their use as PDT agents (see below). Blue and green light display a low tissue penetration depth (1–1.4 mm), which precludes the use of PSs sensitive to short-wavelength visible light for the treatment of deep-seated tumours. Nonetheless, this type of light stimulus combined with interstitial delivery of light is advantageous to avoid damage on healthy, underlying tissue. Indeed, the Ru(II) PS TLD-1433, with a light excitation wavelength of 520 nm, is in clinical trials for the treatment of bladder cancer [13,59]. On the other hand, excitation at higher energy wavelengths (UV) is impractical, due to its limited tissue penetration along with its light-induced cytotoxicity [60,61].

In general, the emission of complexes with general formula [Ir(CˆN)$_2$(NˆN′)]$^+$ takes place from the lowest lying triplet state (T_1), which is formed by a combination of ^{3}MLCT/^{3}LLCT and ^{3}LC states. The emission spectra of our complexes exhibited a band with vibronic structure (two maxima), indicating a major ^{3}LC (^{3}π-π*) character for the transition to the ground state as corroborated by theoretical calculations (Figs. 5(B) and SI-32(B)) [55,62–64]. The higher energy maximum appears between 479 and 511 nm for complexes of series A and between 454 and 468 nm for complexes of series B. Hence, the observed maximum wavelengths (λ_{max}) for **[1b] Cl** - **[4b] Cl** are blue-shifted relative to those recorded for **[1a] Cl** – **[4a] Cl**, which reveals an increase of the $S_0 \leftarrow T_1$ energy attributed to the presence of the -F atoms on the CˆN ligands as predicted by our calculations and reported in the literature [65–67]. Moreover, the presence of alkyl-amide groups on the NˆN′ ligand results in a hypsochromic shift compared to the respective complex with an alkyl-ketone substituent in both series (32 nm in series A and 14 nm in series B). Triplet energy levels (E_T) are directly calculated from the maximum emission peaks (Table 3) and are critical parameters for efficient energy transfer (ET) to $^3O_2$ in the generation of $^1O_2$. Indeed, molecular oxygen (O_2) has two singlet excited states ($^1\Sigma_g$ and $^1\Delta_g$) with

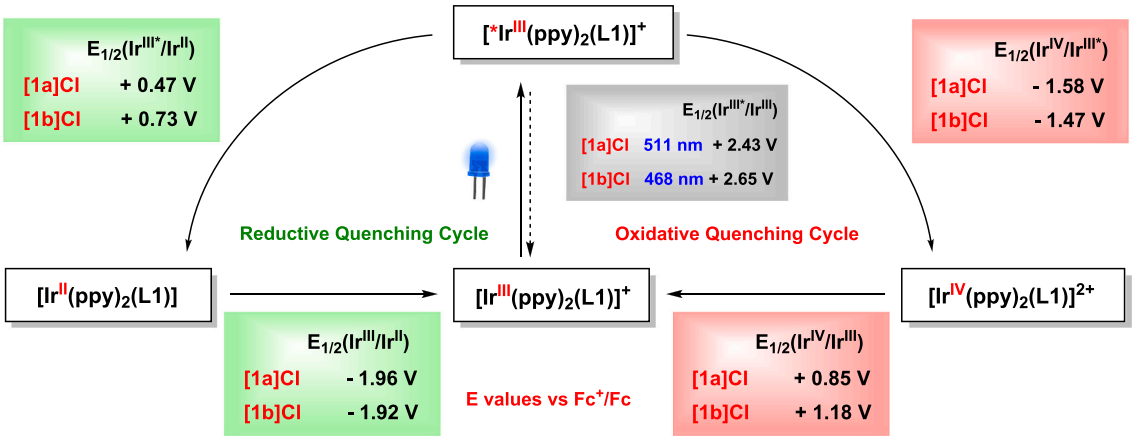

Fig. 4. Latimer diagrams for **[1a] Cl** and **[1b] Cl** with redox potentials determined by CV and the emission energy calculated from the photoluminescence spectrum. The redox potentials for **[1a]** $^{+}$-**[1b]** $^{+}$ and its excited states **[1a*]** $^{+}$-**[1b*]** $^{+}$ are given in V versus Fc^{+}/Fc. $E_{1/2}(Ir^{IV}/Ir^{III*}) = E_{1/2}(Ir^{IV}/Ir^{III})$ - $E_{1/2}(Ir^{III*}/Ir^{III})$ and $E_{1/2}(Ir^{III*}/Ir^{II}) = E_{1/2}(Ir^{III}/Ir^{II}) + E_{1/2}(Ir^{III*}/Ir^{III})$. All the potential values are given as reduction potentials regardless the sense of the arrows for the quenching cycles.

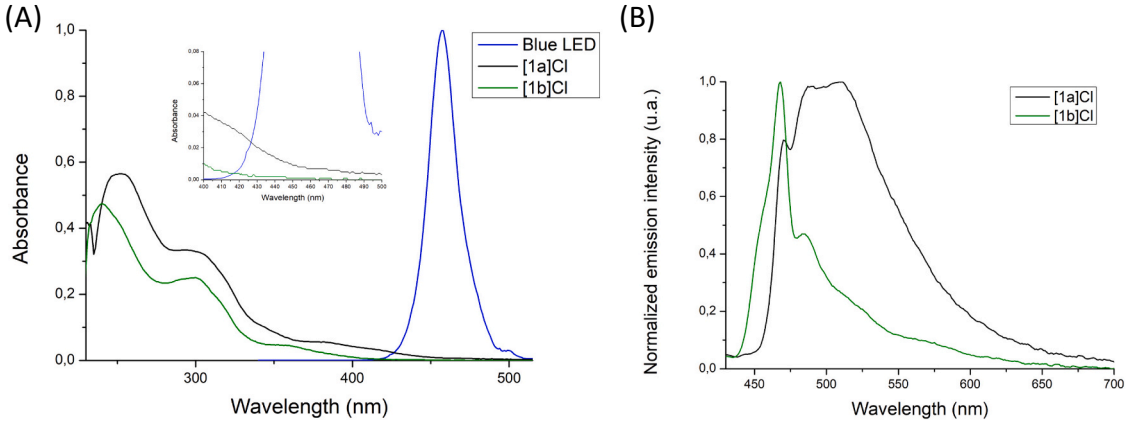

Fig. 5. (A) Overlaid UV–Vis absorption spectra of complexes **[1a] Cl** and **[1b] Cl** (10^{-5} M) in H_2O-DMSO (94:6, v:v) at 25 °C, together with the emission band recorded for the blue light source used in biological experiments (overlapping region in the inset). **(B)** Overlaid emission spectra of complexes **[1a] Cl** and **[1b] Cl** in H_2O-DMSO (94:6, v:v) (10^{-5} M) at 25 °C under a nitrogen atmosphere (λ_{ex} = 405 nm). (For interpretation of the references to colour in this figure legend, the reader is referred to the web version of this article.)

Table 3
Photophysical properties for complexes **[1a] Cl** - **[4a] Cl** to **[1b] Cl** - **[4b] Cl** determined in H_2O-DMSO (94:6, v:v) (10^{-5} M) at 25 °C under a nitrogen atmosphere with λ_{ex} = 405 nm.

Complex	λ_{abs}(nm)	ε [M^{-1} cm^{-1}]	ε [M^{-1} cm^{-1}] (at 460 nm)	λ_{em}(nm) [E_T(eV)]	Φ_{PL} (%)	τ (ns)
[1a] Cl	252, 295, 382	56,500, 33,400, 5600	900	511 [2.43 eV]	9	13
[2a] Cl	242, 295, 373	56,400, 31,500, 5400	600	479 [2.59 eV], 506	8	265
[3a] Cl	242, 295, 381	42,600, 29,900, 4800	300	479 [2.59 eV], 505	7	358
[4a] Cl	241, 297, 373	38,800, 26,400, 4300	200	479 [2.59 eV], 505	3	356
[1b] Cl	240, 300, 357	47,400, 25,100, 4600	100	468 [2.65 eV]	0.03	-
[2b] Cl	240, 294, 355	41,700, 22,000, 5100	600	454 [2.73 eV], 482	0.13	-
[3b] Cl	240, 300, 357	50,400, 31,100,5800	200	454 [2.73 eV], 482	0.52	-
[4b] Cl	240, 300, 365	42,500, 25,900, 4100	100	454 [2.73 eV], 482	0.08	-

absorption energies of 762 nm (1.63 eV) and 1268 nm (0.98 eV), respectively, so that the triplet energy level of an efficient $^1O_2$ photosensitizer has to be higher than these values. Concurrently, PSs with extremely high triplet energy values bring about inefficient ET owing to mismatch with the energy levels of $^1O_2$ [68]. Therefore, we speculate that **[1a] Cl**, with the lowest triplet energy value (2.43 eV), could be the most appropriate $^1O_2$ photosensitizer in this family of complexes.

The emission quantum yields (PLQY, Φ_{PL}) were experimentally determined in H_2O-DMSO (94:6, v:v) and are low for **[1a] Cl** - **[4a] Cl** (3–9%) and very low for **[1b] Cl** - **[4b] Cl** (< 1%) (Table 3). On the other hand, the excited state lifetimes (τ) are only given for complexes of series A in H_2O-DMSO (94:6, v:v), due to the low Φ_{PL} values obtained for derivatives of series B. The replacement of the -CH_2COPh group in **[1a] Cl** with different -CH_2CONR_2 groups in **[2a] Cl** - **[4a] Cl**, results in longer τ values (Table 3), likely as a result of the energy-gap law [69–71].

3.8. *Ability of $^1O_2$ generation*

Singlet oxygen is considered as the main cytotoxic species in Type II PDT [72]. Moreover, DPBF is widely reckoned as a $^1O_2$ capture agent [73]. Therefore, the ability to generate singlet oxygen ($^1O_2$) was demonstrated for **[1a] Cl** and **[3a] Cl** in acetonitrile by recording the

evolution of the respective UV–Vis spectra during the oxidation of DPBF (yellow) to 1,2-dibenzoylbenzene (colorless) in the presence of our photosensitizers under blue light irradiation (λ_{ir} = 460 nm) at 1 s intervals for a total exposure period of 8 s (Fig. 6). Both kinetic experiments showed a decay in the intensity of DPBF consistent with the generation of $^1O_2$. A control experiment for the photooxidation of DPBF in acetonitrile under blue light irradiation in the absence of PS was also performed. In line with the results obtained by Li et al. [74] in other solvents, we observed that DPBF undergoes a certain degree of photooxidation under these conditions, although the rate is remarkably lower than those recorded in the presence of **[1a] Cl** and **[3a] Cl** (Table SI-9).

Considering the experimental results and the bibliographic background [21], we postulate that our complexes can operate through a photochemical pathway consisting of several steps: (a) Photoexcitation of the Ir-PS from their ground state to the singlet excited state ($[Ir^{III}] \rightarrow {}^1[Ir^{III}]^*$); (b) formation of the Ir long-lived triplet excited state via intersystem crossing (${}^1[Ir^{III}]^* \rightarrow {}^3[Ir^{III}]^*$); generation of $^1O_2$ by mean of an energy transfer step (${}^3[Ir^{III}]^* + {}^3O_2 \rightarrow [Ir^{III}] + {}^1O_2$). Alternatively, ${}^3[Ir^{III}]^*$ could generate the radical anion superoxide ($O_2^{\bullet -}$) through an electron transfer pathway, since we have proved that superoxide levels are increased upon treatment with photoactivated complexes (*vide infra*).

3.9. Phototoxic activity and cellular uptake

In order to assess the potential of these compounds for cancer PDT, their cytotoxic activity against PC-3 prostate cancer cells was assessed in the dark or upon irradiation with a blue light (λ_{ir} = 460 nm) for 1 h. The light dose applied (24.1 J cm^{-2}) was similar to that used to photoactivate other Ir-based PSs [45]. Compounds were tested at concentrations up to 50 μM and the concentration that inhibits the viability of cells by 50% (IC_{50}) was determined after 48 h of treatment using an MTT assay. All compounds exhibited a cytotoxic effect against PC-3 cells in the absence of irradiation, with IC_{50} values between 12.76 μM and 2.75 μM (Table 4). These values are in the range of cisplatin, a well-established anticancer agent, assayed under the same conditions (Table 4). Upon light irradiation, compounds **[1a] Cl** – **[4a] Cl** exhibited a marked increase in their cytotoxic activity, with IC_{50} values between 0.32 μM and 2.36 μM. In particular, the highest phototoxicity index values (PI = $IC_{50,dark}/IC_{50,light}$) were obtained for **[1a] Cl** (PI: 8.6) and **[3a] Cl** (PI: 7.5) while **[2a] Cl** and **[4a] Cl** displayed lower PI values of 4.5 and 4.2, respectively. In contrast, the activity of compounds **[1b] Cl** – **[4b] Cl** was essentially not enhanced by light irradiation. Only **[4b] Cl** showed higher activity upon irradiation, with a moderate PI of 2.3. As afore-suggested, the negligible or weak photoactivation of complexes **[1b] Cl** – **[4b] Cl** is likely related to their weaker absorption in the visible region of the spectrum and in particular in the blue light region.

Table 4
Cytotoxic activity against PC-3 cells.

Compound	$IC_{50,dark}$(μM)	$IC_{50,light}$(μM)	PI[a]
[1a] Cl	2.75 ± 0.37	0.32 ± 0.10	8.6
[2a] Cl	10.52 ± 1.17	2.36 ± 0.46	4.5
[3a] Cl	12.76 ± 0.44	1.71 ± 0.75	7.5
[4a] Cl	3.90 ± 1.13	0.92 ± 0.12	4.2
[1b] Cl	4.52 ± 0.02	1.94 ± 0.52	2.3
[2b] Cl	6.32 ± 0.73	6.01 ± 1.06	1.1
[3b] Cl	6.32 ± 0.48	5.57 ± 0.32	1.1
[4b] Cl	4.64 ± 1.21	4.75 ± 0.09	1.0
Cisplatin	2.53 + 0.73	–	–

PC-3 cells were exposed to the compounds in the dark or with light irradiation (1 h, 6.7 mW cm^{-2}, λ_{ir} = 460 nm). IC_{50} values were determined 48 h later by an MTT assay. Data represents the mean ± SD of at least two independent experiments, each performed in triplicate. [a] PI: phototoxicity index = $IC_{50,dark}/IC_{50,light}$.

In addition, the excited state lifetime seems not to be the determining factor in the PI value for our complexes, as **[1a] Cl** exhibits the lowest value of all these photosensitizers. We postulate that the higher phototoxicity of **[1a] Cl** compared to its congeners could be related to its good absorption profile in the blue light region, its appropriate E_T value and its ability to generate $^1O_2$ (vide supra).

Based on these results, complexes **[1a] Cl** and **[3a] Cl**, which hold the highest potential for PDT, were chosen for further investigations on their biological action mechanism.

An efficient accumulation of the PS into target cells is crucial to achieve an effective phototherapy. By contrast, low cellular uptake is widely regarded as one of the main causes of resistance to chemotherapy [6]. Taking advantage of the intrinsic fluorescence of **[1a] Cl** and **[3a] Cl**, their cellular internalization was characterized by flow cytometry. First, the uptake kinetics of the complexes were determined to assess the optimal incubation time to ensure their accumulation into the cells prior to photoactivation. To this end, PC-3 cells were exposed to **[1a] Cl** and **[3a] Cl** at 5 μM for 1, 4, 6 and 16 h and the percentage of cells with green fluorescence emission, corresponding to the uptake of the complexes, was determined relative to non-treated cells. Uptake kinetic curves were obtained by fitting the measured data points to one-phase exponential association curves with GraphPad Software (Fig. 7). The plateau values of the kinetic curves were similar for both complexes, indicating they have the same ability to internalize into cells. However, the estimated half-time to reach the plateau was lower for **[1a] Cl** (1.41 h) than for **[3a] Cl** (4.28 h), revealing that **[1a] Cl** has a faster internalization rate.

Based on the uptake kinetics, the cytotoxic effect of **[1a] Cl** and **[3a] Cl** was further evaluated, extending the incubation time before irradiation up to 6 h. In addition, SK-MEL-28 melanoma cells and non-malignant CCD-18Co fibroblasts, as healthy control cells, were

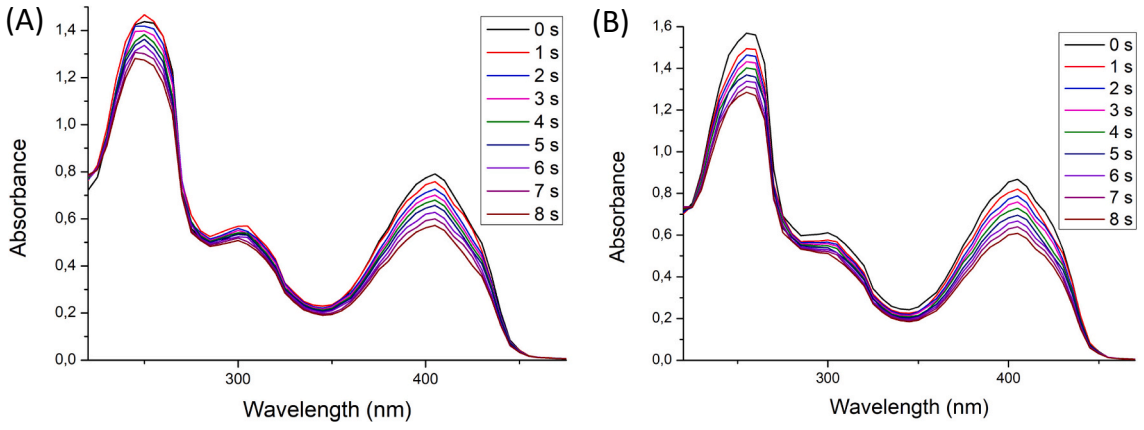

Fig. 6. Photocatalytic oxidation of DPBF under blue light in the presence of **[1a] Cl** (A) and **[3a] Cl** (B) in acetonitrile.

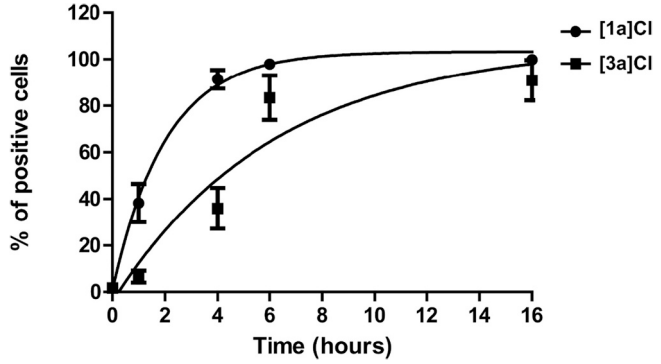

Fig. 7. Internalization kinetics of compounds **[1a] Cl** and **[3a] Cl**. PC-3 cells were incubated with the compounds at 5 μM for 1, 4, 6, and 16 h at 37 °C and the % of cells with positive fluorescence relative to control untreated cells was determined by flow cytometry. Data represents the mean ± SD of three independent experiments.

included in the study (Table 5). The longer preincubation time resulted in a higher phototoxicity against PC-3 cells, with $IC_{50,light}$ values of 0.22 ± 0.03 for **[1a] Cl** and 0.88 ± 0.24 μM for **[3a] Cl.** These values are 1.4 and 1.9 fold lower than those obtained for **[1a] Cl** and **[3a] Cl** after 1 h of preincubation (Table 4). Notably, **[1a] Cl** and **[3a] Cl** exhibited high cytotoxicity against SK-MEL-28 cells in the dark and, more importantly, after irradiation (Table 5), resulting in a PI of 23.4 for **[1a] Cl** and 21.4 for **[3a] Cl**. The cytotoxic activity of the complexes in the dark or upon photoactivation against cancer cells is comparable to that of other families of Ir(III) complexes [11,19,57,75,76]. In contrast, their activity against non-tumoral CCD18-Co fibroblasts was moderate, with $IC_{50,dark}$ values of 5.87 ± 0.66 μM and 24.06 ± 2.92 μM and $IC_{50,light}$ values of 0.54 ± 0.10 μM and 3.39 ± 1.31 μM, for **[1a] Cl** and **[3a] Cl** respectively, revealing a lower toxic effect against healthy cells. The Selective Phototoxicity Indexes (SPI) of these complexes were calculated by comparing the $IC_{50,dark}$ values in non-malignant cells to the $IC_{50,light}$ values in cancer cells ($IC_{50,dark}$ CCD-18Co/$IC_{50,light}$ cancer cells). It should be noted that in the case of SK-MEL-28 cells, an SPI value of 117.4 was obtained for **[1a] Cl** and of 171.8 for **[3a] Cl**. These results indicate that in the clinical setting, the PS dose required for a melanoma PDT-based treatment would not be toxic to healthy cells since they are not exposed to irradiation. Moreover, it is worth mentioning that neither of the two compounds displayed hemolytic activity against red blood cells at the $IC_{50,dark}$ (Table 5) or even at concentrations up to 25 μM (data not shown).

3.10. Clonogenic assay

The long-term effectiveness of **[1a] Cl** and **[3a] Cl** was determined by measuring their capacity to inhibit the ability of single cells to survive and reproduce to form colonies. Cisplatin was used as positive control. PC-3 cells were incubated for 6 h with the complexes at their corresponding $IC_{50,light}$ and then kept in the dark or photoactivated for 1 h. Cells were immediately plated at low density and allowed to grow and form colonies for 10 days. Then, the colony number in each plate was determined. As shown in Fig. 8, a significant reduction of the number of colonies was observed in cells exposed to photoactivated **[1a] Cl** and **[3a] Cl** compared to control cells (90.0 ± 1.31% and 98.8 ± 0.20% of inhibition, respectively). These values are similar to those observed for cisplatin (89.8 ± 3.7%). In contrast, the clonogenicity of the cells was only inhibited by 18.2 ± 3.8% and by 21.4 ± 4.8% when the treatments with **[1a] Cl** and **[3a] Cl**, respectively, were performed in the dark.

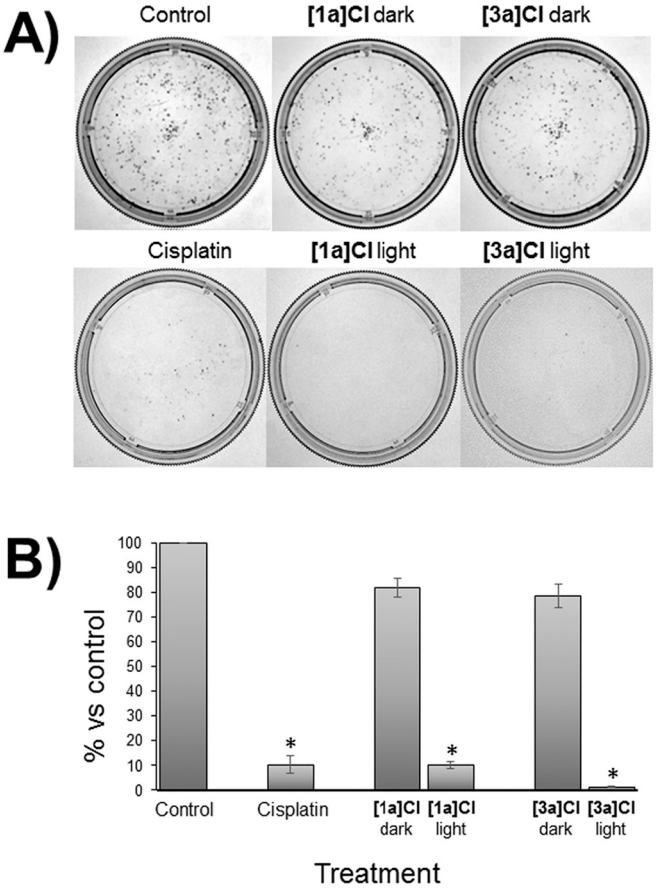

Fig. 8. Clonogenic assay. (A) Colony formation of PC-3 cells after exposure to **[1a] Cl** or **[3a] Cl** at the $IC_{50,light}$ in the dark or under photoactivation. Control cells were treated with medium alone. Cisplatin was used as a positive control. (B) Bar charts represent the percentage of colonies relative to control untreated cells after each treatment (mean ± SD of 3 experiments. *$p < 0.05$ versus control cells).

Table 5
Cytotoxic activity against PC-3 and SK-MEL-28 cancer cells and CCD-18Co fibroblasts.

Compound:	[1a] Cl				[3a] Cl			
	IC_{50}(μM)		PI[a]	SPI[b]	IC_{50}(μM)		PI[a]	SPI[b]
Cell line:	Dark	Light			Dark	Light		
PC-3	2.75 ± 0.37	0.22 ± 0.03	12.5	26.7	12.76 ± 0.44	0.88 ± 0.24	14.5	27.3
SK-MEL-28	1.17 ± 0.28	0.05 ± 0.01	23.4	117.4	2,99 ± 0.23	0.14 ± 0.02	21.4	171.8
CCD-18Co	5.87 ± 0.66	0.54 ± 0.10	10.9		24.06 ± 2.92	3.39 ± 1.31	7.3	
Hemolysis[c]	< 5%				< 5%			

Cells were preincubated with the compounds for 6 h to allow the cellular uptake and then irradiated with a blue light (6.7 mW cm^{-2}, λ_{ir} = 460 nm) or incubated in the dark for 1 h. IC_{50} values were determined 48 h later by an MTT assay. Data represents the mean ± SD of at least two independent experiments, each performed in triplicate. [a] PI: phototoxicity index = $IC_{50,dark}/IC_{50,light}$. [b] SPI: Selective Phototoxicity Index = $IC_{50,dark}$ CCD-18Co/$IC_{50,light}$ cancer cells. [c] Percentage of hemolysis at the $IC_{50,dark}$.

These results point out that the photodynamic activity of these complexes can greatly reduce the number of cells with tumorigenic capacity.

3.11. Internalization mechanism and intracellular localization

To know the cellular uptake mechanism of a potential drug is important for its therapeutic or diagnostic applications. It may require energy, as for endocytosis and active transport mediated by proteins, or be energy-independent, as happens in passive diffusion through the membrane or diffusion facilitated by channels and carriers. For instance, different reports have shown that Ir(III) complexes can be internalized into the cells by energy independent pathways [77], non-endocytotic energy dependent pathways [78], or endocytosis [79].

To establish the internalization mechanism of **[1a]Cl** and **[3a]Cl**, PC-3 cells were incubated with the compounds at 5 μM for 1 h: i) at 37 °C, to allow any possible cellular uptake mechanism; ii) at 4 °C, to inhibit processes that require metabolic energy, and iii) at 37 °C after pre-incubation with dynasore, an specific inhibitor of endocytosis. After 1 h of incubation at 37 °C, the median fluorescence intensity (MFI) of the cells significantly increased (from 8,511 ± 706 in control cells to 20,425 ± 2,525 in cells exposed to **[1a]Cl** and to 13,330 ± 34 in cells incubated with **[3a]Cl**), demonstrating an efficient cellular uptake of the compounds. However, these fluorescence levels were reduced by 87.3% and 92.2% respectively when cells were incubated at 4 °C (Fig. 9), indicating that the compounds are mainly internalized through an energy-dependent mechanism. In addition, pre-treatment with dynasore almost completely abolished the internalization of both compounds. Dynasore is a cell-permeable molecule that inhibits activity of dynamin, a protein involved in vesicle scission from plasma membrane during endocytosis [80]. Thus, it can be concluded that **[1a]Cl** and **[3a]Cl**

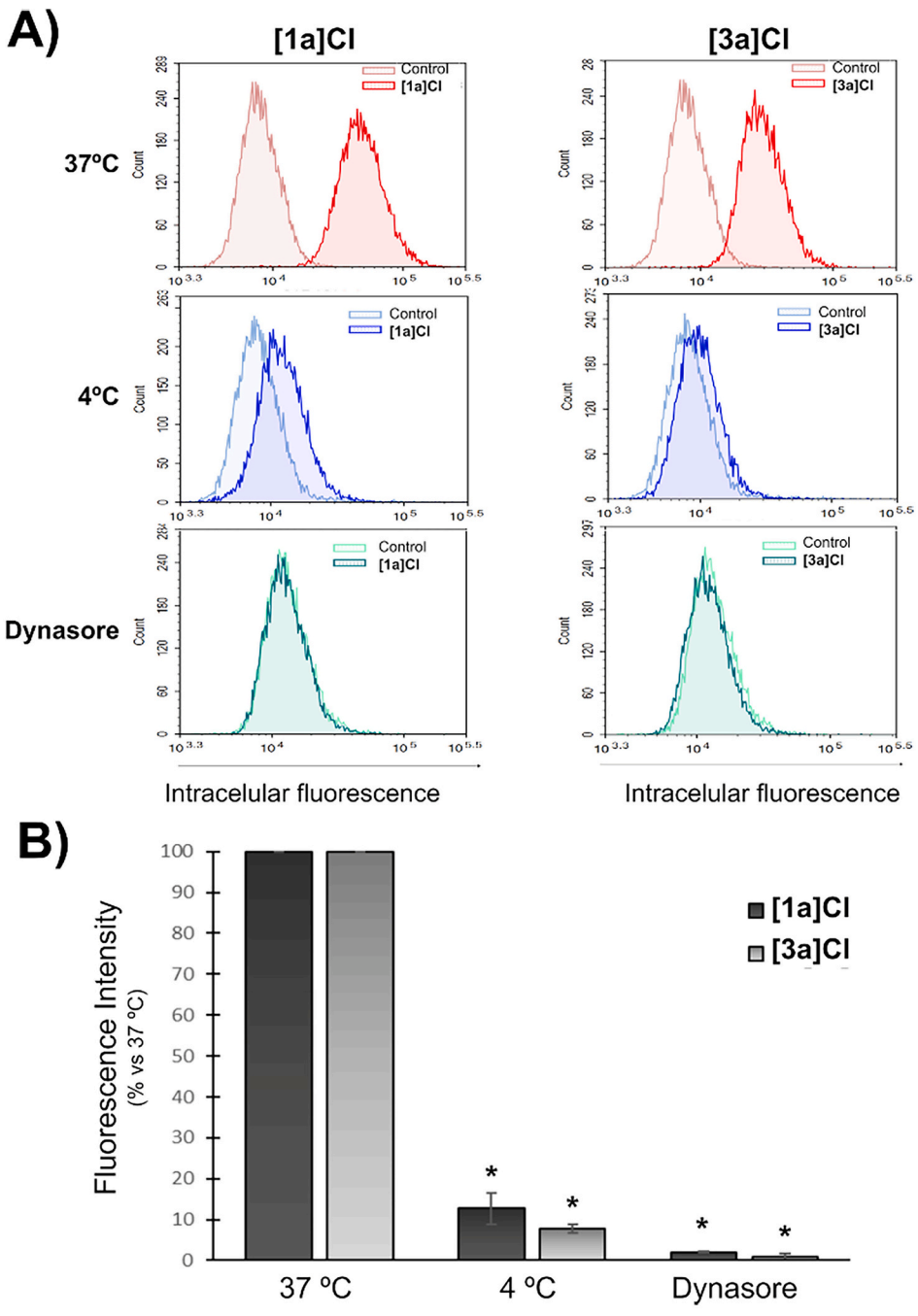

Fig. 9. Cellular uptake mechanism study for **[1a]Cl** and **[3a]Cl.** PC-3 cells were incubated with the compounds at 5 μM or medium alone as a control for 1 h under different conditions: at 37 °C, at 4 °C (metabolic inhibition), and at 37 °C after dynasore pre-incubation (endocytosis inhibition). The MFI of the cells, corresponding to the intracellular uptake of the peptides, was determined by flow cytometry. (A) Representative flow cytometry histograms obtained for control cells and for cells incubated with **[1a]Cl** and **[3a]Cl**. (B) Percentage of intracellular fluorescence at the different conditions in comparison to cells incubated at 37 °C. Each bar represents the mean fluorescence intensity of at least two independent experiments ± SD. *$p < 0.05$ vs cells treated at 37 °C.

enter the cells principally by endocytosis. Moreover, the experiments were performed in serum free culture medium and therefore, the endocytosis of the compounds is not assisted by serum lipids or proteins.

The intracellular localization of a PS is an important factor for the outcome of PDT since ROS have a short half-life and act close to their site of generation [81]. Therefore, the cellular damage induced by the compounds is highly dependent on their localization inside the cells. To obtain more insight into the subcellular localization of **[1a] Cl** and **[3a] Cl** confocal microscopy experiments were performed after exposing SK-MEL-28 cells to the compounds for 1 h. Colocalization studies with mitochondria were conducted by co-staining the cells with the red-fluorescent dye MitoTracker™ Red CMXRos.

As shown in Fig. 10(A), a punctuated green fluorescent staining was observed in cells exposed to **[1a] Cl** and **[3a] Cl**, indicating the accumulation of the compounds throughout the cytoplasm of the cells. In contrast, no fluorescence particles were detected inside the cell nucleus. Merged images of **[1a] Cl** or **[3a] Cl** and MitoTracker™ Red revealed a high degree of colocalization, which can be seen in yellow, with Pearson correlation coefficients of 0.908 and 0.809, respectively. The Mander's overlap coefficient between **[1a] Cl** and MitoTracker™ Red was 0.861 indicating that a high fraction of the complex colocalize with mitochondria. However, a lower Mander's coefficient was obtained for **[3a] Cl** (M: 0.55) revealing a lower degree of colocalization. In Fig. 10(B), a higher magnification image of **[3a] Cl** confirms that although the green particles are mainly located in the mitochondria, the complex is also detected in other subcellular locations, which point out that it can accumulate in other organelles, such as lysosomes or endoplasmic reticulum (ER) as described for other iridium complexes [7]. These findings were further confirmed by a multichannel plot, where the Y-axis represents the fluorescence intensity of the green and red channels in each pixel of the image selected by the white line and the X-axis shows the horizontal distance of the line (Fig. 10(B)). Changes in the intensity plots were synchronous for both channels along the line revealing a good colocalization except in the perinuclear area, where only green fluorescence was detected. Overall, these results showed that **[1a] Cl** and **[3a] Cl** mainly accumulate into the mitochondria in agreement with previous reports describing that positively charged cyclometalated Ir (III) complexes with moderate lipophilic character tend to accumulate within these organelles, even in the absence of specific targeting groups. This fact seems to be favoured by the negative potential of mitochondrial membranes [24,26,82,83]. Thus, these PSs show excellent properties for their potential application as probes in bioimaging of mitochondria, in particular **[1a] Cl**.

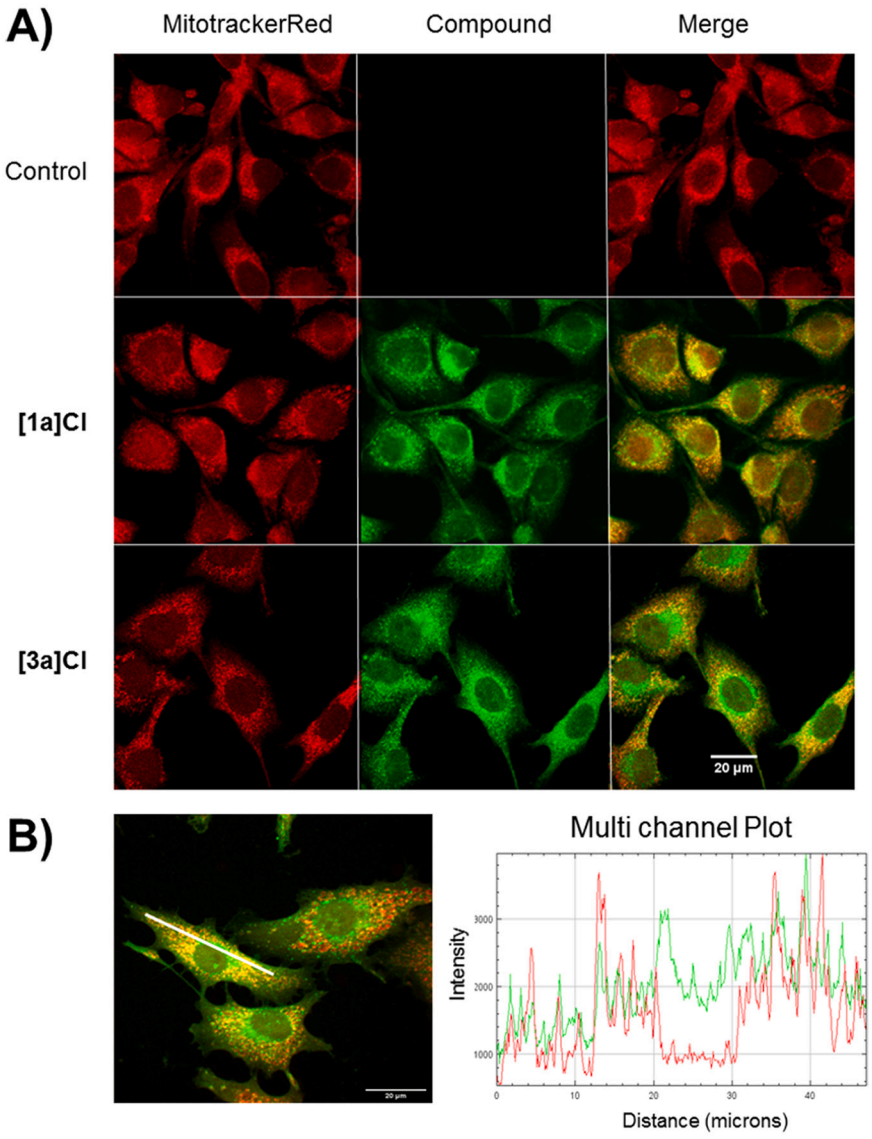

Fig. 10. Confocal microscopic imaging of the subcellular localization of **[1a] Cl** and **[3a] Cl**. SK-MEL-28 cells were incubated with the compounds at 25 µM or with medium alone (control) for 1 h at 37 °C. Mitochondria were stained with MitoTrackerRed™. (A) The localization of the compounds is indicated by the green fluorescence (excitation wavelength: 400 nm; emission wavelength: 525 nm). Mitochondria staining is shown by the red fluorescence (excitation wavelength: 543 nm; emission wavelength: 595 nm). Colocalization can be observed in yellow in the merged images. (B) High magnification image showing **[3a] Cl** and MitotrackerRed co-staining. The multichannel plot (right) represents the green and red fluorescence intensity in each pixel of the merged image indicated by the white line. (For interpretation of the references to colour in this figure legend, the reader is referred to the web version of this article.)

3.12. Superoxide production

The radical anion superoxide is considered the most important ROS in cells [84]. We analysed the ability of these complexes to generate this radical at the cellular level using a specific fluorescent probe. PC-3 cells were incubated with **[1a]Cl** and **[3a]Cl** for 6 h at the corresponding $IC_{50,light}$ and then kept in the dark or photoactivated. The formation of superoxide radicals was immediately measured by flow cytometry (Fig. 11). The MFI of the cells increased by 1.46 ± 0.61-fold and by 1.42 ± 0.54-fold compared to control cells when exposed to photoactivated **[1a]Cl** and **[3a]Cl** respectively, revealing an increase of the intracellular superoxide levels. In contrast, the MFI of the cells was not altered when treated with the complexes in the dark. Overall, these results confirm that the photodynamic activity of **[1a]Cl** and **[3a]Cl** generates ROS at cellular level, which is in agreement with the photochemical mechanism proposed above.

3.13. Mitochondrial damage

Mitochondrial membrane potential (MMP) is an indicator of mitochondrial activity and is essential for ATP production, cellular metabolism, cell signalling and redox balance [85]. In order to assess whether the photodynamic activity of **[1a]Cl** and **[3a]Cl** interferes with the MMP, as reported for other Ir complexes [86,87], mitochondrial membrane depolarization was monitored by flow cytometry using the JC-1 dye. In healthy cells, JC-1 exhibits an MMP-dependent accumulation in the mitochondria as aggregates that display a red fluorescence. However, when the mitochondrial membrane is depolarized, JC-1 remains in the cytosol as a monomer that emits green fluorescence. The ratio of this green/red fluorescence depends only on the MMP, as no fluorescence emission was detected in cells incubated with the complexes at the $IC_{50,light}$ without the JC-1 (Fig. SI-47). In control cells, a red emission from JC-1 aggregates was detected together with a green fluorescence corresponding to JC-1 monomers (Fig. 12). A similar fluorescence pattern was observed in PC-3 cells exposed to **[1a]Cl** and **[3a]Cl** in the dark, indicating that the MMP was preserved. However, the emission of JC-1 shifted from red to green upon irradiation of the cells in the presence of **[1a]Cl** and **[3a]Cl** revealing the depolarization

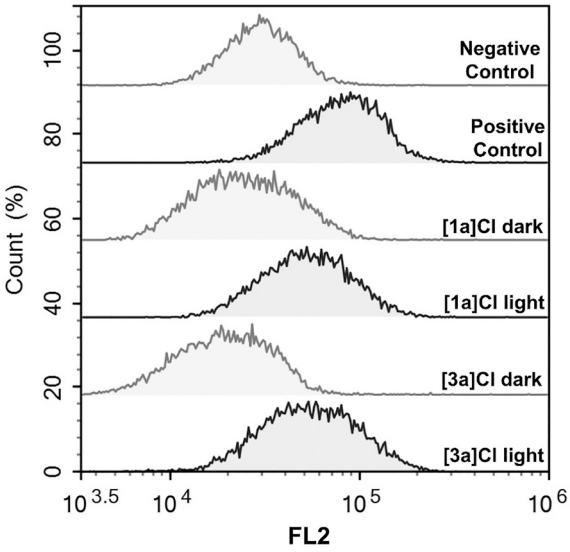

Fig. 11. Superoxide generation by **[1a]Cl** and **[3a]Cl** in PC-3 cells. Cells were incubated with the complexes at the $IC_{50,light}$ for 6 h and then kept in the dark or photoactivated for 1 h. Pyocyanin was used as ROS inducer (positive control). Non-treated cells were used as negative control. Superoxide generation was monitored with a commercial fluorescent probe. Representative flow cytometry histograms show the MFI of 10,000 cells in the FL2 channel.

of the mitochondrial membrane in more than 90% of the cells. Similar results were obtained after the treatment of the cells with CCCP, a classical mitochondrial uncoupler that increases the proton permeability across the mitochondrial inner membrane, dissipating the transmembrane potential. These results reveal that the photodynamic activity of both **[1a]Cl** and **[3a]Cl** causes a mitochondrial dysfunction that can lead to cell death.

3.14. Photocatalytic oxidation of NADH

NAD is a coenzyme that exists in both the oxidized (NAD^+) and the reduced (NADH) forms and is involved in diverse biochemical redox processes. For instance, in the mitochondrial electron transport chain, complex I (NADH dehydrogenase) oxidizes NADH to NAD^+ and the electrons are transported through a series of proteins and electron carriers to O_2 in a process that concurrently pumps protons across the mitochondrial inner membrane. This process generates a proton gradient between the matrix and the intermembrane space, which is mainly responsible for the MMP and drives the ATP synthesis in eukaryotic cells (oxidative phosphorylation) [88]. Thus, the alteration of the mitochondrial NADH/NAD^+ ratio may disrupt the electron transport chain and trigger cell death [89]. In two recent reports, the groups of Huang [17] and Sadler [89] have proved the activity of Ir(III) complexes on the photooxidation of NADH.

Thus, we studied the photocatalytic oxidation of NADH (100 μM) in methanol/H_2O (1:1, *v*/v, 2500 μL) in the presence of **[1a]Cl** (5 μM) under air and blue light exposure (λ_{ir} = 460 nm), by monitoring the evolution of the respective UV–Vis spectrum at room temperature during 24 h (Fig. 13). No symptoms of reaction were observed during the first 30 min. However, after 24 h the band centred at 339 nm (maximum of NADH) underwent a remarkable decrease, while the band at 259 nm (maximum of NAD^+) experienced an increase, in agreement with the oxidation of NADH. The turnover number and turnover frequency values were 6.23 and 0.26 h^{-1}. The photocatalytic nature of this process was verified by mean of control experiments. Indeed, no oxidation was observed either in the absence of PS or in the dark after 24 h (Figure SI-45 and SI-46). As a result, we concluded that the photocatalytic ability of **[1a]Cl** could contribute to the afore-mentioned mitochondrial membrane depolarization. Therefore, we postulate that NADH might be one of the molecular targets in mitochondria and that the impairment of the redox homeostasis stemming from its oxidation could also trigger apoptosis.

3.15. Reaction with DNA

Cytotoxicity of traditional metal-based anticancer drugs is often associated with genomic DNA damage and cell cycle perturbation. By contrast, mitochondria have been found to be the major target of **[1a]Cl** and **[3a]Cl**. Thus, we explored whether the photodynamic activity of the complexes can affect mtDNA. In fact, circular mtDNA has been shown to be more susceptible to ROS damage than nuclear DNA [90].

The ability of **[1a]Cl** and **[3a]Cl** to interfere with DNA was first explored by electrophoretic mobility assays, which analyse the mobility shift of circular plasmid DNA due to an alteration of its conformation [91]. The plasmid used (pUC18) naturally has a supercoiled conformation (SC) with a high electrophoretic mobility. Under the action of damaging agents, such as ROS, the plasmid can suffer a single strand break that generates an open circular conformation (OC) with reduced electrophoretic mobility, or a double strand break that leads to a linear form with an intermediate mobility. When the damage is severe, DNA can be greatly fractionated, and fractions are eluted from the gel undetected.

The activity of **[1a]Cl** and **[3a]Cl** on DNA cleavage was assayed in the dark and under irradiation at concentrations ranging from 0 to 100 μM, based on a previous study [92]. A treatment with 1.75% H_2O_2 and 20 μM $FeCl_2$ was used as positive control of ROS generation and nuclease

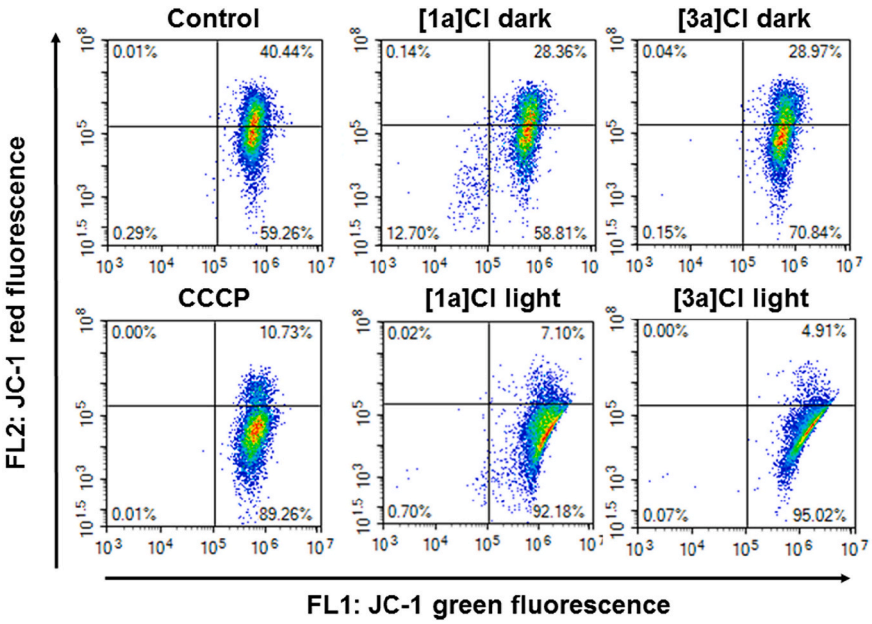

Fig. 12. Flow cytometry analysis of the mitochondrial membrane potential (MMP) after treatment with **[1a] Cl** and **[3a] Cl** using the JC-1 dye. PC-3 cells were incubated with medium alone as a control or with the compounds at the corresponding $IC_{50,light}$ in the dark or with light irradiation. CCCP, a mitochondrial uncoupler, was used as a control drug to induce a membrane depolarization. Plots represent fluorescence intensities of green JC-1 monomers (FL1) and red JC-1 aggregates (FL2) in the cells. The % population of positive cells is given in the respective quadrants. Reduced red fluorescence indicates decreased MMP. (For interpretation of the references to colour in this figure legend, the reader is referred to the web version of this article.)

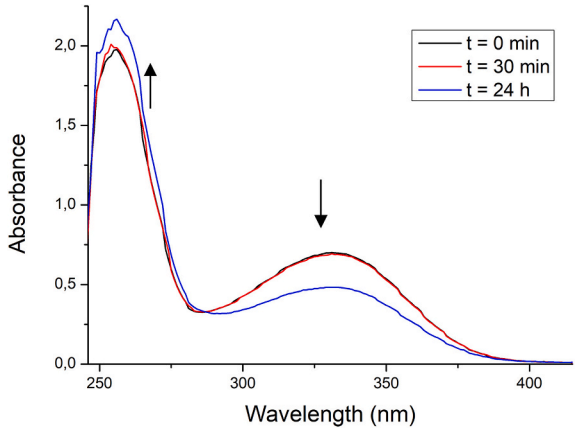

Fig. 13. Evolution of the UV–Vis spectrum of NADH (100 μM) in MeOH/H_2O (1:1, v/v, 2.5 mL) in the presence of **[1a] Cl** (5 μM) under air and blue light exposure (λ_{ir} = 460 nm) at room temperature. during 24 h. (For interpretation of the references to colour in this figure legend, the reader is referred to the web version of this article.)

activity. As shown in Fig. 14(A), neither of the compounds altered the electrophoretic mobility of the plasmid at 10 μM. At 25 μM and 50 μM of either **[1a] Cl** or **[3a] Cl**, the ratio between OC and SC forms of plasmid was slightly higher in the irradiated samples than in samples incubated in the absence of light. Moreover, the total amount of DNA decreased at treatments from 50 μM, being completely degraded at 75 μM under irradiation and at 100 μM in the dark, indicating a strong nuclease activity under these conditions.

In order to analyse whether ROS are involved in the nuclease activity of the complexes, treatments at 70 μM were performed in the presence of ROS scavengers (sodium azide as a scavenger of singlet oxygen, DMSO as a scavenger of hydroxyl radical, and Tiron as a scavenger of the superoxide radical anion) [93]. As shown in Fig. 14(B), DNA degradation caused by **[1a] Cl** was completely reverted by sodium azide and DMSO, and almost completely reverted by tiron both in the dark and under irradiation. The damage cause by **[3a] Cl** was completely reverted by the three ROS scavengers in both conditions, although DMSO was slightly less efficient in the dark. Overall, the oxidative activity of the compounds under irradiation appears to be modestly higher since some OC conformations are present, indicating that scavengers could not completely reverse the effect of the ROS. These results point out to an oxidative damage mechanism for Ir(III) complexes involving different ROS that could affect mtDNA among other target molecules in the mitochondria.

The interaction of the complexes with mtDNA was further evaluated at the cellular level. In particular, the impact of **[1a] Cl** and **[3a] Cl** on the transcription levels of genes *ND3* and *COX1*, which are located in the mitochondrial genome, was quantitatively assessed by RT-qPCR. *ND3* encodes the NADH dehydrogenase subunit 3 of the respiratory chain complex I and *COX1* (or *CO1*) encodes the cytochrome *c* oxidase subunit I of the complex IV. Changes in the expression of these genes were normalized using the housekeeping gene β-actin (*ACTB*) as a reference. The quantification cycle (Cq) values for *ACTB* in control cells (18.98 ± 0.49) and cells treated with **[1a] Cl** (18.64 ± 0.81) or **[3a] Cl** (18.80 ± 0.33) showed no statistical differences. As shown in Fig. 15, PC-3 cells exposed to **[1a] Cl** or **[3a] Cl** with photoactivation showed a significative reduction in the expression of both mitochondrial genes in comparison to control cells, which is a consequence of mtDNA damage. In particular, the expression of *ND3* was reduced by 31 ± 6% and 35 ± 3% after **[1a] Cl** and **[3a] Cl** treatments, respectively, while the expression of *COX1* was reduced by 44 ± 4% in cells exposed to **[1a] Cl,** reaching a 72 ± 2% reduction in cells exposed to **[3a] Cl.**

Thus, these results confirm that **[1a] Cl** and **[3a] Cl** can damage mtDNA at cellular level and hence affect mitochondrial functions [76].

We also observed that photoactivated **[1a] Cl** and **[3a] Cl** induced a minimal effect on cell cycle progression, as assessed by propidium iodide staining and flow cytometry analysis after 24 h of treatment (Fig. SI-48). In contrast, cisplatin, whose mode of action is mediated by the interaction with nuclear DNA, generated a marked cell cycle arrest at the S and G2/M phases [94,95]. These results support that the nuclease activity of the complexes is most likely restricted to mtDNA, in agreement with their subcellular distribution.

3.16. Cell death mechanism

Finally, we studied the cell death mechanism induced by photoactivated **[1a] Cl** and **[3a] Cl** by flow cytometry using the annexin V/propidium iodide dual staining protocol. Annexin V identifies apoptotic cells by its ability to bind to phosphatidylserine, a marker of apoptosis

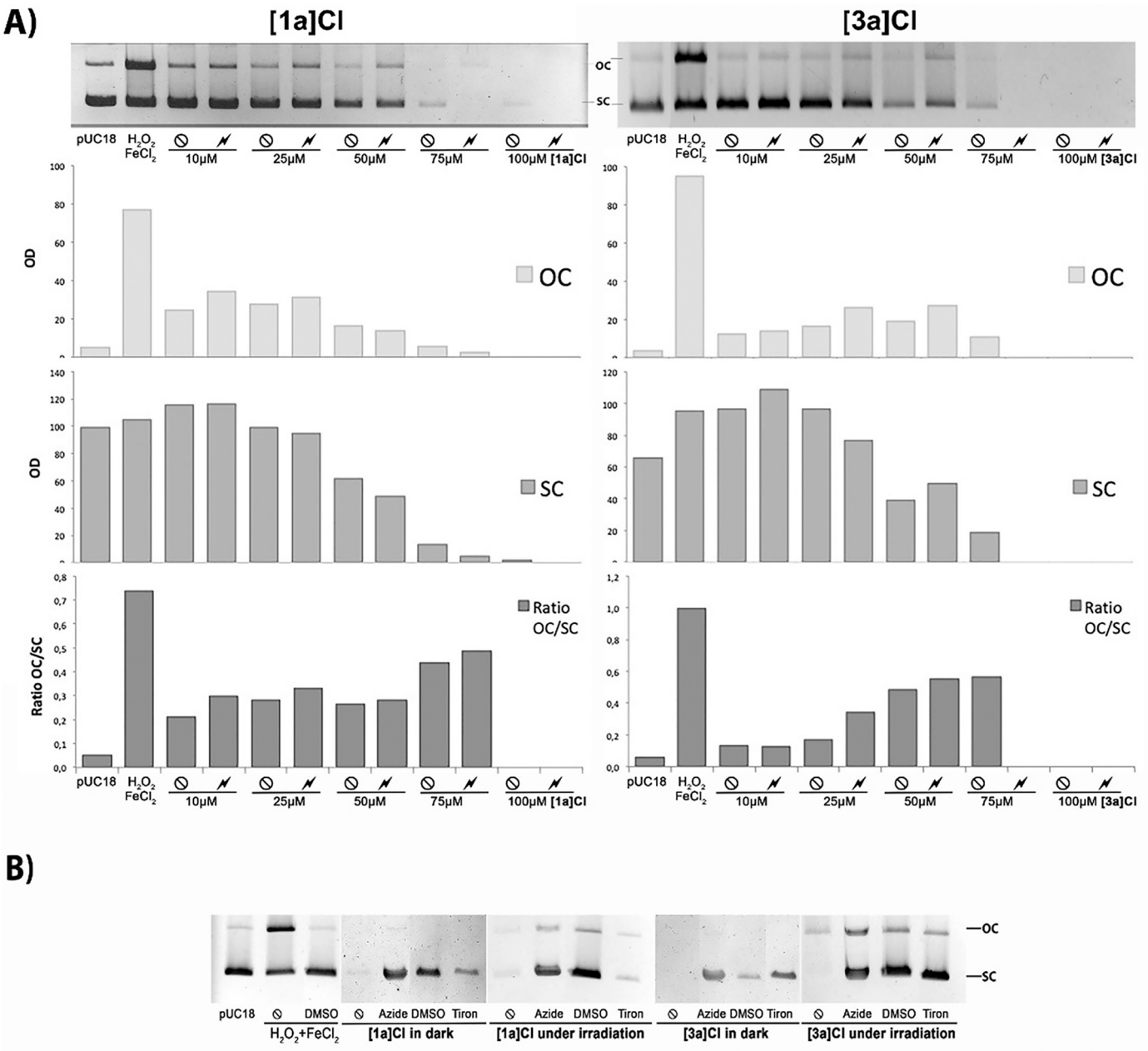

Fig. 14. Electrophoretic mobility assay. The specific treatments are indicated under each lane. pUC18 lane shows the electrophoretic pattern of the untreated plasmid. (A) Effect of irradiation on the activity on DNA of **[1a] Cl** and **[3a] Cl**. ⃠ states for the incubation in dark conditions and 🗲 states for the incubation under irradiation. Graphs represent the densitometric analysis of the bands corresponding to the (open circular conformation (OC) and supercoiled conformation (SC) of the plasmid and the ratio between both conformations. (B) Analysis of ROS involved in the mechanism of action of compounds **[1a] Cl** and **[3a] Cl**, at 70 μM, incubated in the dark or after 1 h of irradiation. ⃠ indicates that no scavenger was used in that specific treatment. (SC): supercoiled plasmid conformation. (OC): open circular conformation.

when it is on the outer side of the plasma membrane. Propidium iodide label the cellular DNA in necrotic cells or late apoptotic cells when the integrity of the membranes has been lost. After 24 h of treatment with photoactivated **[1a] Cl** and **[3a] Cl** at their respective $IC_{50,light}$, 26.9% and 22.6% of the cells were positive for both annexin V and propidium iodide staining, whereas only 3.96% of control cells and 12.11% of cells exposed to cisplatin showed a dual staining (Fig. 16). Double stained cells are frequently considered in late apoptosis, but necrosis is also possible. Since **[1a] Cl** and **[3a] Cl** generate mitochondrial membrane depolarization, they can induce an apoptotic response by leakage of cytochrome *c* into the cytosol in response to the depolarization, with subsequent caspase activation [81]. However, increasing oxidative damage may finally lead to the plasma membrane permeabilization and a secondary necrosis [96]. Thus, the complexes could induce a dual cell apoptotic/necrotic death response upon light irradiation.

4. Conclusions

In conclusion, with the objective of developing new potential PDT photosensitizers, we have prepared and fully characterized two series of new Ir(III) complexes of general formula $[Ir(C^N)_2(N^N')]Cl$, using two different C^N ligands (ppy and dfppy) and four different N^N′ ligands, which share the thiabendazole scaffold but show diverse N-alkyl groups. The complexes are partially soluble in aqueous media and keep their

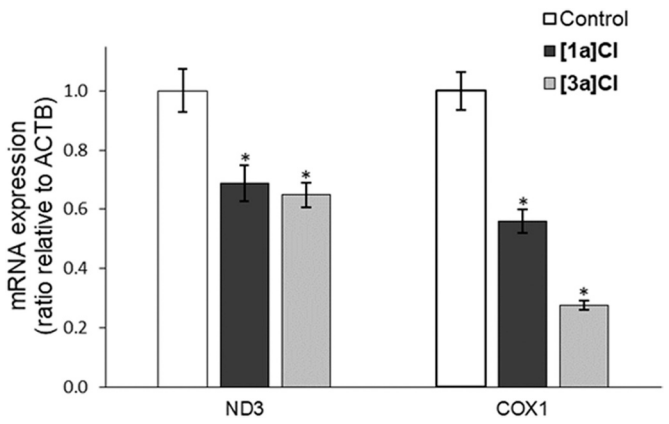

Fig. 15. Relative gene expression of the mitochondrial genes *ND3* and *COX1* in control untreated cells PC-3 and cells incubated with **[1a] Cl** or **[3a] Cl** at the corresponding $IC_{50,light}$ under photoactivated conditions. *β-actin* (*ACTB*) was used as a reference gene. Four RT-qPCR analysis were conducted in two independent biological replicates. Error bars represent SD for the eight assays. $*p <$ 0.05 vs cells control.

integrity under irradiation with blue light for 6 h. Moreover, we have analysed the electrochemical and photophysical properties of the Ir(III) dyes and interpreted the observed trends with the help of theoretical calculations. More specifically, the new PSs feature suitable $S_0 \leftarrow T_1$ energy values to generate $^1O_2$, as well as appropriate excited state redox potentials to produce $O_2^{\bullet-}$. We have also evaluated the cytotoxic activity of the new derivatives in the dark and under blue light illumination. As a result, we have established a correlation between the lack of photocytotoxicity found for derivatives of series B and their absorption profile, which is strongly determined by the presence of -F atoms on the CˆN ligands. By contrast, complexes of series A with more suited absorption profiles in the visible region, display high PI values, as for instance, PI = 23.4 for **[1a] Cl** and PI = 21.4 for **[3a] Cl** in SK-MEL-28 melanoma cells, at concentrations in the nanomolar range. Furthermore, the activity of the lead complexes **[1a] Cl** and **[3a] Cl** against non-tumoral CCD18-Co fibroblasts was moderate, disclosing a high degree of selectivity, as expressed by the Selective Phototoxicity Index (SPI) ($IC_{50,dark}$ CCD-18Co/$IC_{50,light}$ cancer cells) calculated for **[1a] Cl** (SPI = 117.4) and **[3a] Cl** (SPI = 171.8) in SK-MEL-28 with regard to CCD-18Co cells.

Regarding the biological mechanism of action, we have unveiled that **[1a] Cl** and **[3a] Cl** are internalized by energy-dependent endocytosis and that after 6 h of incubation they have been taken up by most of the

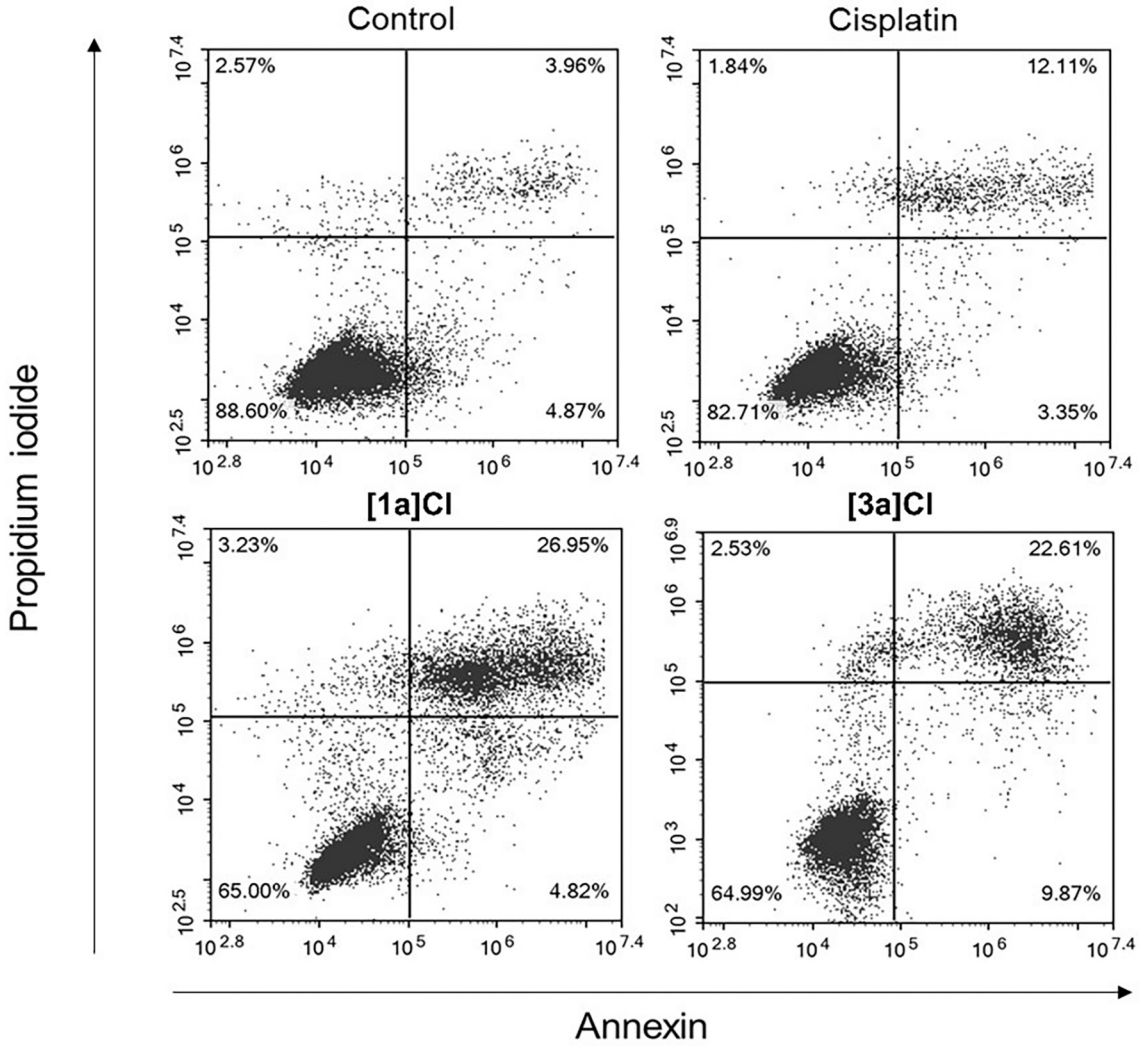

Fig. 16. Cell death mechanism. PC-3 cells were treated with medium alone as a control, cisplatin at 25 μM or with **[1a] Cl** and **[3a] Cl** at the $IC_{50,light}$ and photoactivated. After 24 h, cells were double stained with propidium iodide and Annexin V-FITC and analysed by flow cytometry. The x-axis shows annexin V-FITC staining and the y-axis shows propidium iodide staining. The percentage of cells in each quadrant is indicated.

cells. In addition, they are accumulated primarily within mitochondria. Indeed, we presume that specially **[1a] Cl** offers potential as probe for bioimaging these organelles. More importantly, both PSs trigger a multi-targeted cytotoxic effect through a photocatalytic mechanism that induces the formation of ROS. We have proved that upon irradiation of both PS, the mitochondrial membrane undergoes depolarization, though the MMP is preserved in the dark. We believe that the ability of **[1a] Cl** to photo-catalyse the oxidation of NADH to NAD^+ might contribute to the membrane depolarization. Moreover, **[1a] Cl** and **[3a] Cl** are able to cause severe cleavage on mtDNA, resulting in the inhibition of the expression of mitochondrial genes, so that we postulate that mtDNA is another of their cellular targets. We have revealed that **[1a] Cl** and **[3a] Cl** induce a minimal effect on cell cycle progression, in agreement with their inability to target nuclear DNA. As a result of the multimodal damage to mitochondria, we have found that **[1a] Cl** and **[3a] Cl** elicit a dual cell death response involving both apoptosis and necrosis. In addition, the long-term effect of our PSs was substantiated by performing clonogenic assays, which revealed the great capacity of the drugs to reduce the number of cells capable of reproducing and generate new colonies.

To sum up, we believe that the mitochondrial-targeted phototoxicity displayed by **[1a] Cl** and **[3a] Cl** represents a promising approach in the development of new metal-based PDT agents to treat cancers refractory to conventional chemotherapy.

Author statement-author contributions

Igor Echevarría: Investigation and methodology.
Elisenda Zafon: Investigation, Methodology.
Silvia Barrabés: Investigation, Writing - Review & Editing.
María Ángeles Martínez: Investigation.
Sonia Ramos-Gómez: Investigation (RT-qPCR experiments)
Natividad Ortega: Conceptualization, Investigation (RT-qPCR experiments)
Blanca R. Manzano: Conceptualization, Writing - Original Draft.
Félix A. Jalón: Project administration, Funding acquisition.
Roberto Quesada: Formal analysis (X-ray analysis).
Gustavo Espino: Conceptualization, Methodology, Writing - Original Draft, Supervision, Project administration, Funding acquisition, Visualization.
Anna Massaguer: Conceptualization, Methodology, Writing - Original Draft, Supervision, Project administration, Funding acquisition, Visualization.

Declaration of Competing Interest

The authors declare that they have no known competing financial interests or personal relationships that could have appeared to influence the work reported in this paper.

Acknowledgements

We acknowledge the financial support provided by the Spanish Ministerio de Ciencia, Innovación y Universidades (RTI2018-100709-B-C21, RTI2018-100709-B-C22) and CTQ (QMC)-RED2018-102471-T), Junta de Castilla y León (BU087G19), Junta de Comunidades de Castilla-La Mancha-FEDER (JCCM) (grant SBPLY/19/180501/000260) and UCLM-FEDER (grants 2019-GRIN-27183 and 2019-GRIN-27209). I. Echevarría wants to acknowledge his fellowship to both the European Social Fund and Consejería de Educación de la Junta de Castilla y León (EDU/1100/2017). E. Zafon wants to acknowledge her predoctoral fellowship to the Generalitat de Catalunya (AGAUR; 2021 FI_B 01036).

We are also indebted to Jacinto Delgado, Pilar Castroviejo and Marta Mansilla (PCT of the Universidad de Burgos) for technical support and José Vicente Cuevas Vicario for advice and support with theoretical calculations and Gabriel García-Herbosa for providing us access to CV equipment.

Appendix A. Supplementary data

Supplementary data to this article can be found online at https://doi.org/10.1016/j.jinorgbio.2022.111790.

References

[1] P. Agostinis, K. Berg, K.A. Cengel, T.H. Foster, A.W. Girotti, S.O. Gollnick, S. M. Hahn, M.R. Hamblin, A. Juzeniene, D. Kessel, M. Korbelik, J. Moan, P. Mroz, D. Nowis, J. Piette, B.C. Wilson, J. Golab, Photodynamic therapy of cancer: an update, CA, Cancer J. Clin. 61 (2011) 250–281, https://doi.org/10.3322/caac.20114.
[2] S. Kwiatkowski, B. Knap, D. Przystupski, J. Saczko, E. Kędzierska, K. Knap-Czop, J. Kotlińska, O. Michel, K. Kotowski, J. Kulbacka, Photodynamic therapy – mechanisms, photosensitizers and combinations, Biomed. Pharmacother. 106 (2018) 1098–1107, https://doi.org/10.1016/j.biopha.2018.07.049.
[3] S. Monro, K.L. Colón, H. Yin, J. Roque, P. Konda, S. Gujar, R.P. Thummel, L. Lilge, C.G. Cameron, S.A. McFarland, Transition metal complexes and photodynamic therapy from a tumor-centered approach: challenges, opportunities, and highlights from the development of TLD1433, Chem. Rev. 119 (2019) 797–828, https://doi.org/10.1021/acs.chemrev.8b00211.
[4] T.J. Dougherty, J.E. Kaufman, A. Goldfarb, K.R. Weishaupt, D. Boyle, A. Mittleman, Photoradiation therapy for the treatment of malignant tumors, Cancer Res. 38 (1978) 2628–2635. http://www.ncbi.nlm.nih.gov/pubmed/667856.
[5] V. Novohradsky, A. Rovira, C. Hally, A. Galindo, G. Vigueras, A. Gandioso, M. Svitelova, R. Bresolí-Obach, H. Kostrhunova, L. Markova, J. Kasparkova, S. Nonell, J. Ruiz, V. Brabec, V. Marchán, Towards novel photodynamic anticancer agents generating superoxide anion radicals: a cyclometalated Ir III complex conjugated to a far-red emitting coumarin, Angew. Chem. Int. Ed. 58 (2019) 6311–6315, https://doi.org/10.1002/anie.201901268.
[6] V. Novohradsky, L. Markova, H. Kostrhunova, J. Kasparkova, J. Ruiz, V. Marchán, V. Brabec, A cyclometalated Ir III complex conjugated to a coumarin derivative is a potent photodynamic agent against prostate differentiated and tumorigenic cancer stem cells, Chem. – A Eur. J. 27 (2021) 8547–8556, https://doi.org/10.1002/chem.202100568.
[7] C.P. Tan, Y.M. Zhong, L.N. Ji, Z.W. Mao, Phosphorescent metal complexes as theranostic anticancer agents: combining imaging and therapy in a single molecule, Chem. Sci. 12 (2021) 2357–2367, https://doi.org/10.1039/d0sc06885c.
[8] L. He, Y. Li, C.-P. Tan, R.-R. Ye, M.-H. Chen, J.-J. Cao, L.-N. Ji, Z.-W. Mao, Cyclometalated iridium(<scp>iii</scp>) complexes as lysosome-targeted photodynamic anticancer and real-time tracking agents, Chem. Sci. 6 (2015) 5409–5418, https://doi.org/10.1039/C5SC01955A.
[9] A. Zamora, G. Vigueras, V. Rodríguez, M.D. Santana, J. Ruiz, Cyclometalated iridium(III) luminescent complexes in therapy and phototherapy, Coord. Chem. Rev. 360 (2018) 34–76, https://doi.org/10.1016/j.ccr.2018.01.010.
[10] J. Pracharova, G. Vigueras, V. Novohradsky, N. Cutillas, C. Janiak, H. Kostrhunova, J. Kasparkova, J. Ruiz, V. Brabec, Exploring the effect of polypyridyl ligands on the anticancer activity of phosphorescent iridium(III) complexes: from proteosynthesis inhibitors to photodynamic therapy agents, Chem. - A Eur. J. 24 (2018) 4607–4619, https://doi.org/10.1002/chem.201705362.
[11] V. Novohradsky, G. Vigueras, J. Pracharova, N. Cutillas, C. Janiak, H. Kostrhunova, V. Brabec, J. Ruiz, J. Kasparkova, Molecular superoxide radical photogeneration in cancer cells by dipyridophenazine iridium(<scp>iii</scp>) complexes, Inorg. Chem. Front. 6 (2019) 2500–2513, https://doi.org/10.1039/C9QI00811J.
[12] C.-S. Tan, N.B. Kumarakulasinghe, Y.-Q. Huang, Y. Li, E. Ang, J. Rou, En Choo, B.-C. Goh, R.A. Soo, Third Generation EGFR TKIs: Current Data and Future Directions, 2022, https://doi.org/10.1186/s12943-018-0778-0.
[13] X. Li, J.F. Lovell, J. Yoon, X. Chen, Clinical development and potential of photothermal and photodynamic therapies for cancer, Nat. Rev. Clin. Oncol. 17 (2020) 657–674, https://doi.org/10.1038/s41571-020-0410-2.
[14] P. Chinna Ayya Swamy, G. Sivaraman, R.N. Priyanka, S.O. Raja, K. Ponnuvel, J. Shanmugpriya, A. Gulyani, Near infrared (NIR) absorbing dyes as promising photosensitizer for photo dynamic therapy, Coord. Chem. Rev. 411 (2020), 213233, https://doi.org/10.1016/j.ccr.2020.213233.
[15] L.K. McKenzie, I.V. Sazanovich, E. Baggaley, M. Bonneau, V. Guerchais, J.A. G. Williams, J.A. Weinstein, H.E. Bryant, Metal complexes for two-photon photodynamic therapy: a cyclometallated iridium complex induces two-photon photosensitization of cancer cells under near-IR light, Chem. - A Eur. J. 23 (2017) 234–238, https://doi.org/10.1002/chem.201604792.
[16] P.M. Shah, H. Gerdes, Endoscopic options for early stage esophageal cancer, J. Gastrointest. Oncol. 6 (2015) 20–30, https://doi.org/10.3978/j.issn.2078-6891.2014.096.
[17] C. Huang, C. Liang, T. Sadhukhan, S. Banerjee, Z. Fan, T. Li, Z. Zhu, P. Zhang, K. Raghavachari, H. Huang, In-vitro and in-vivo photocatalytic cancer therapy with biocompatible iridium(III) photocatalysts, Angew. Chem. Int. Ed. 60 (2021) 9474–9479, https://doi.org/10.1002/anie.202015671.
[18] J. Zhao, K. Yan, G. Xu, X. Liu, Q. Zhao, C. Xu, S. Gou, An iridium (III) complex bearing a donor–acceptor–donor type ligand for NIR-triggered dual phototherapy, Adv. Funct. Mater. 31 (2021) 2008325, https://doi.org/10.1002/adfm.202008325.

[19] H. Yuan, Z. Han, Y. Chen, F. Qi, H. Fang, Z. Guo, S. Zhang, W. He, Ferroptosis photoinduced by new cyclometalated iridium(III) complexes and its synergism with apoptosis in tumor cell inhibition, Angew. Chem. Int. Ed. 60 (2021) 8174–8181, https://doi.org/10.1002/anie.202014959.
[20] L. Zhang, Y. Geng, L. Li, X. Tong, S. Liu, X. Liu, Z. Su, Z. Xie, D. Zhu, M.R. Bryce, Rational design of iridium–porphyrin conjugates for novel synergistic photodynamic and photothermal therapy anticancer agents, Chem. Sci. 12 (2021) 5918–5925, https://doi.org/10.1039/D1SC00126D.
[21] A.P. Castano, T.N. Demidova, M.R. Hamblin, Mechanisms in photodynamic therapy: part one—photosensitizers, photochemistry and cellular localization, Photodiagn. Photodyn. Ther. 1 (2004) 279–293, https://doi.org/10.1016/S1572-1000(05)00007-4.
[22] S. Tornroth-Horsefield, R. Neutze, Opening and closing the metabolite gate, Proc. Natl. Acad. Sci. 105 (2008) 19565–19566, https://doi.org/10.1073/pnas.0810654106.
[23] N.L. Oleinick, R.L. Morris, I. Belichenko, The role of apoptosis in response to photodynamic therapy: what, where, why, and how, Photochem. Photobiol. Sci. 1 (2002) 1–21, https://doi.org/10.1039/b108586g.
[24] J. Zielonka, J. Joseph, A. Sikora, M. Hardy, O. Ouari, J. Vasquez-Vivar, G. Cheng, M. Lopez, B. Kalyanaraman, Mitochondria-targeted triphenylphosphonium-based compounds: syntheses, mechanisms of action, and therapeutic and diagnostic applications, Chem. Rev. 117 (2017) 10043–10120, https://doi.org/10.1021/acs.chemrev.7b00042.
[25] Y. Li, C.-P. Tan, W. Zhang, L. He, L.-N. Ji, Z.-W. Mao, Phosphorescent iridium(III)-bis-N-heterocyclic carbene complexes as mitochondria-targeted theranostic and photodynamic anticancer agents, Biomaterials 39 (2015) 95–104, https://doi.org/10.1016/j.biomaterials.2014.10.070.
[26] C. Pérez-Arnaiz, M.I. Acuña, N. Busto, I. Echevarría, M. Martínez-Alonso, G. Espino, B. García, F. Domínguez, Thiabendazole-based Rh(III) and Ir(III) biscyclometallated complexes with mitochondria-targeted anticancer activity and metal-sensitive photodynamic activity, Eur. J. Med. Chem. 157 (2018) 279–293, https://doi.org/10.1016/j.ejmech.2018.07.065.
[27] E. Zafón, I. Echevarría, S. Barrabés Vera, B.R. Manzano, F.A. Jalon, A. M. Rodríguez, A. Massaguer, G. Espino, Photodynamic therapy with mitochondria-targeted biscyclometalated Ir(III) complexes. Multi-action mechanism and strong influence of the cyclometallating ligand, Dalton Trans. (2021), https://doi.org/10.1039/D1DT03080A.
[28] J. Torres, M.C. Carrión, J. Leal, F.A. Jalón, J.V. Cuevas, A.M. Rodríguez, G. Castañeda, B.R. Manzano, Cationic bis(cyclometalated) Ir(III) complexes with pyridine–carbene ligands. Photophysical properties and photocatalytic hydrogen production from water, Inorg. Chem. 57 (2018) 970–984, https://doi.org/10.1021/acs.inorgchem.7b02289.
[29] Y. Chen, L. Qiao, L. Ji, H. Chao, Phosphorescent iridium(III) complexes as multicolor probes for specific mitochondrial imaging and tracking, Biomaterials 35 (2014) 2–13, https://doi.org/10.1016/j.biomaterials.2013.09.051.
[30] R.R. Ye, C.P. Tan, L. He, M.H. Chen, L.N. Ji, Z.W. Mao, Cyclometalated Ir(III) complexes as targeted theranostic anticancer therapeutics: combining HDAC inhibition with photodynamic therapy, Chem. Commun. 50 (2014) 10945–10948, https://doi.org/10.1039/c4cc05215c.
[31] G.R. Fulmer, A.J.M. Miller, N.H. Sherden, H.E. Gottlieb, A. Nudelman, B.M. Stoltz, J.E. Bercaw, K.I. Goldberg, NMR chemical shifts of trace impurities: common laboratory solvents, organics, and gases in deuterated solvents relevant to the organometallic chemist, Organometallics 29 (2010) 2176–2179, https://doi.org/10.1021/om100106e.
[32] M. Nonoyama, Benzo[h]quinolin-10-yl-N iridium(III) complexes, Bull. Chem. Soc. Jpn. 47 (1974) 767–768, https://doi.org/10.1246/bcsj.47.767.
[33] N. Adarsh, R.R. Avirah, D. Ramaiah, Tuning photosensitized singlet oxygen generation efficiency of novel Aza-BODIPY dyes, Org. Lett. 12 (2010) 5720–5723, https://doi.org/10.1021/ol102562k.
[34] P. Majumdar, X. Yuan, S. Li, B. Le Guennic, J. Ma, C. Zhang, D. Jacquemin, J. Zhao, Cyclometalated Ir(III) complexes with styryl-BODIPY ligands showing near IR absorption/emission: preparation, study of photophysical properties and application as photodynamic/luminescence imaging materials, J. Mater. Chem. B 2 (2014) 2838–2854, https://doi.org/10.1039/C4TB00284A.
[35] S.P.Y. Li, C.T.S. Lau, M.W. Louie, Y.W. Lam, S.H. Cheng, K.K.W. Lo, Mitochondria-targeting cyclometalated iridium(III)-PEG complexes with tunable photodynamic activity, Biomaterials 34 (2013) 7519–7532, https://doi.org/10.1016/j.biomaterials.2013.06.028.
[36] I. Mäger, E. Eiríksdóttir, K. Langel, S. EL Andaloussi, Ü. Langel, Assessing the uptake kinetics and internalization mechanisms of cell-penetrating peptides using a quenched fluorescence assay, Biochim. Biophys. Acta Biomembr. 1798 (2010) 338–343, https://doi.org/10.1016/j.bbamem.2009.11.001.
[37] S. Bolte, F.P. Cordelières, A guided tour into subcellular colocalization analysis in light microscopy, J. Microsc. 224 (2006) 213–232, https://doi.org/10.1111/j.1365-2818.2006.01706.x.
[38] M.W. Pfaffl, A new mathematical model for relative quantification in real-time RT-PCR, Nucleic Acids Res. 29 (2001) 45e–45, https://doi.org/10.1093/nar/29.9.e45.
[39] W. Liu, Z. Gong, K. Zhang, W. Dong, H. Zou, R. Song, J. Bian, J. Zhu, G. Liu, Z. Liu, Paeonol protects renal tubular cells against cadmium-induced cytotoxicity via alleviating oxidative stress, inhibiting inflammatory responses and restoring autophagy, J. Inorg. Biochem. 230 (2022), 111733, https://doi.org/10.1016/j.jinorgbio.2022.111733.
[40] W.-K. Huang, C.-W. Cheng, S.-M. Chang, Y.-P. Lee, E.W.-G. Diau, Synthesis and electron-transfer properties of benzimidazole-functionalized ruthenium complexes for highly efficient dye-sensitized solar cells, Chem. Commun. 46 (2010) 8992, https://doi.org/10.1039/c0cc03517c.
[41] M. Vaquero, N. Busto, N. Fernández-Pampín, G. Espino, B. García, Appended aromatic moieties determine the cytotoxicity of neutral cyclometalated platinum (II) complexes derived from 2-(2-Pyridyl)benzimidazole, Inorg. Chem. 59 (2020) 4961–4971, https://doi.org/10.1021/acs.inorgchem.0c00219.
[42] E.C. Constable, M. Neuburger, P. Rösel, G.E. Schneider, J.A. Zampese, C. E. Housecroft, F. Monti, N. Armaroli, R.D. Costa, E. Ortí, Ligand-based charge-transfer luminescence in ionic cyclometalated iridium(III) complexes bearing a pyrene-functionalized bipyridine ligand: a joint theoretical and experimental study, Inorg. Chem. 52 (2013) 885–897, https://doi.org/10.1021/ic302026f.
[43] B.J. Coe, M. Helliwell, J. Raftery, S. Sánchez, M.K. Peers, N.S. Scrutton, Cyclometalated Ir(<scp>iii</scp>) complexes of deprotonated N-methylbipyridinium ligands: effects of quaternised N centre position on luminescence, Dalton Trans. 44 (2015) 20392–20405, https://doi.org/10.1039/C5DT03753K.
[44] C.E. Elgar, H.Y. Otaif, X. Zhang, J. Zhao, P.N. Horton, S.J. Coles, J.M. Beames, S.J. A. Pope, Iridium(III) sensitisers and energy upconversion: the influence of ligand structure upon TTA-UC performance, Chem. – A Eur. J. 27 (2021) 3427–3439, https://doi.org/10.1002/chem.202004146.
[45] L.K. McKenzie, H.E. Bryant, J.A. Weinstein, Transition metal complexes as photosensitisers in one- and two-photon photodynamic therapy, Coord. Chem. Rev. 379 (2019) 2–29, https://doi.org/10.1016/j.ccr.2018.03.020.
[46] C.D. Sunesh, G. Mathai, Y. Choe, Constructive effects of long alkyl chains on the electroluminescent properties of cationic iridium complex-based light-emitting electrochemical cells, ACS Appl. Mater. Interfaces 6 (2014) 17416–17425, https://doi.org/10.1021/am5058426.
[47] R.D. Costa, E. Ortí, H.J. Bolink, F. Monti, G. Accorsi, N. Armaroli, E. Orti, H. J. Bolink, F. Monti, G. Accorsi, N. Armaroli, Luminescent ionic transition-metal complexes for light-emitting electrochemical cells, Angew. Chem. Int. Ed. 51 (2012) 8178–8211, https://doi.org/10.1002/anie.201201471.
[48] J.M. Dąbrowski, B. Pucelik, A. Regiel-Futyra, M. Brindell, O. Mazuryk, A. Kyzioł, G. Stochel, W. Macyk, L.G. Arnaut, Engineering of relevant photodynamic processes through structural modifications of metallotetrapyrrolic photosensitizers, Coord. Chem. Rev. 325 (2016) 67–101, https://doi.org/10.1016/j.ccr.2016.06.007.
[49] A.F. Henwood, A.K. Bansal, D.B. Cordes, A.M.Z. Slawin, I.D.W. Samuel, E. Zysman-Colman, Solubilised bright blue-emitting iridium complexes for solution processed OLEDs, J. Mater. Chem. C 4 (2016) 3726–3737, https://doi.org/10.1039/C6TC00151C.
[50] C. Momblona, C.D. Ertl, A. Pertegás, J.M. Junquera-Hernández, H.J. Bolink, E. C. Constable, M. Sessolo, E. Ortí, C.E. Housecroft, Exploring the effect of the cyclometallating ligand in 2-(pyridine-2-yl)benzo[d]thiazole-containing iridium(iii) complexes for stable light-emitting electrochemical cells, J. Mater. Chem. C 6 (2018) 12679–12688, https://doi.org/10.1039/C8TC04727H.
[51] D. Tordera, M. Delgado, E. Ortí, H.J. Bolink, J. Frey, M.K. Nazeeruddin, E. Baranoff, Stable green electroluminescence from an iridium tris-heteroleptic ionic complex, Chem. Mater. 24 (2012) 1896–1903, https://doi.org/10.1021/cm3011716.
[52] A.F. Henwood, A.K. Pal, D.B. Cordes, A.M.Z. Slawin, T.W. Rees, C. Momblona, A. Babaei, A. Pertegás, E. Ortí, H.J. Bolink, E. Baranoff, E. Zysman-Colman, Blue-emitting cationic iridium(<scp>iii</scp>) complexes featuring pyridylpyrimidine ligands and their use in sky-blue electroluminescent devices, J. Mater. Chem. C 5 (2017) 9638–9650, https://doi.org/10.1039/C7TC03110F.
[53] H. Iranmanesh, K.S.A. Arachchige, M. Bhadbhade, W.A. Donald, J.Y. Liew, K.T. C. Liu, E.T. Luis, E.G. Moore, J.R. Price, H. Yan, J. Yang, J.E. Beves, Chiral ruthenium(II) complexes as supramolecular building blocks for heterometallic self-assembly, Inorg. Chem. 55 (2016) 12737–12751, https://doi.org/10.1021/acs.inorgchem.6b02007.
[54] N. Demir, M. Karaman, G. Yakali, T. Tugsuz, S. Denizalti, S. Demic, B. Dindar, M. Can, Structure–property relationship in amber color light-emitting electrochemical cell with TFSI counteranion: enhancing device performance by different substituents on N ∧ N ligand, Inorg. Chem. 60 (2021) 4410–4423, https://doi.org/10.1021/acs.inorgchem.0c02939.
[55] M. Martínez-Alonso, J. Cerdá, C. Momblona, A. Pertegás, J.M. Junquera-Hernández, A. Heras, A.M. Rodríguez, G. Espino, H. Bolink, E. Ortí, Highly stable and efficient light-emitting electrochemical cells based on cationic iridium complexes bearing arylazole ancillary ligands, Inorg. Chem. 56 (2017) 10298–10310, https://doi.org/10.1021/acs.inorgchem.7b01167.
[56] R. Bevernaegie, S.A.M. Wehlin, B. Elias, L. Troian-Gautier, A roadmap towards visible light mediated electron transfer chemistry with iridium(III) complexes, ChemPhotoChem. 5 (2021) 217–234, https://doi.org/10.1002/cptc.202000255.
[57] J.-J. Cao, C.-P. Tan, M.-H. Chen, N. Wu, D.-Y. Yao, X.-G. Liu, L.-N. Ji, Z.-W. Mao, Targeting cancer cell metabolism with mitochondria-immobilized phosphorescent cyclometalated iridium(III) complexes, Chem. Sci. 8 (2017) 631–640, https://doi.org/10.1039/C6SC02901A.
[58] S. Takizawa, R. Aboshi, S. Murata, Photooxidation of 1,5-dihydroxynaphthalene with iridium complexes as singlet oxygen sensitizers, Photochem. Photobiol. Sci. 10 (2011) 895–903, https://doi.org/10.1039/c0pp00265h.
[59] J. Karges, Clinical development of metal complexes as photosensitizers for photodynamic therapy of cancer, Angew. Chem. Int. Ed. 61 (2022), https://doi.org/10.1002/anie.202112236.
[60] L.N. Lameijer, D. Ernst, S.L. Hopkins, M.S. Meijer, S.H.C. Askes, S.E. Le Dévédec, S. Bonnet, A red-light-activated ruthenium-caged NAMPT inhibitor remains phototoxic in hypoxic cancer cells, Angew. Chem. Int. Ed. 56 (2017) 11549–11553, https://doi.org/10.1002/anie.201703890.
[61] P. Avci, A. Gupta, M. Sadasivam, Low-level laser (light) therapy (LLLT) in skin: stimulating, healing, restoring, Semin Cutan Med. Surg. 32 (1) (2013) 41–52. https

://www.scmsjournal.com/article/abstract/low-level-laser-light-therapy-lllt-in-skin-stimulating-healing-restoring/.
[62] C.D. Ertl, J. Cerdá, J.M. Junquera-Hernández, A. Pertegás, H.J. Bolink, E. C. Constable, M. Neuburger, E. Ortí, C.E. Housecroft, Colour tuning by the ring roundabout: [Ir(CˆN) 2 (NˆN)] + emitters with sulfonyl-substituted cyclometallating ligands, RSC Adv. 5 (2015) 42815–42827, https://doi.org/10.1039/C5RA07940C.
[63] C.D. Ertl, L. Gil-Escrig, J. Cerdá, A. Pertegás, H.J. Bolink, J.M. Junquera-Hernández, A. Prescimone, M. Neuburger, E.C. Constable, E. Ortí, C.E. Housecroft, Regioisomerism in cationic sulfonyl-substituted [Ir(CˆN) 2 (NˆN)] + complexes: its influence on photophysical properties and LEC performance, Dalton Trans. 45 (2016) 11668–11681, https://doi.org/10.1039/C6DT01325B.
[64] M.-H. Chen, F.-X. Wang, J.-J. Cao, C.-P. Tan, L.-N. Ji, Z.-W. Mao, Light-up mitophagy in live cells with dual-functional theranostic phosphorescent iridium (III) complexes, ACS Appl. Mater. Interfaces 9 (2017) 13304–13314, https://doi.org/10.1021/acsami.7b01735.
[65] P. Coppo, E.A. Plummer, L. De Cola, Tuning iridium(III) phenylpyridine complexes in the “almost blue” region, Chem. Commun. 4 (2004) 1774–1775, https://doi.org/10.1039/b406851c.
[66] J. Torres, M.C. Carrión, J. Leal, F.A. Jalón, J.V. Cuevas, A.M. Rodríguez, G. Castañeda, B.R. Manzano, Cationic bis(cyclometalated) Ir(III) complexes with pyridine–carbene ligands. Photophysical properties and photocatalytic hydrogen production from water, Inorg. Chem. 57 (2018) 970–984, https://doi.org/10.1021/acs.inorgchem.7b02289.
[67] H.J. Bolink, E. Coronado, R.D. Costa, N. Lardiés, E. Ortí, Near-quantitative internal quantum efficiency in a light-emitting electrochemical cell, Inorg. Chem. 47 (2008) 9149–9151, https://doi.org/10.1021/ic801587n.
[68] J.S. Nam, M.-G. Kang, J. Kang, S.-Y. Park, S.J.C. Lee, H.-T. Kim, J.K. Seo, O.-H. Kwon, M.H. Lim, H.-W. Rhee, T.-H. Kwon, Endoplasmic reticulum-localized iridium(III) complexes as efficient photodynamic therapy agents via protein modifications, J. Am. Chem. Soc. 138 (2016) 10968–10977, https://doi.org/10.1021/jacs.6b05302.
[69] T.C. Motley, L. Troian-Gautier, M.K. Brennaman, G.J. Meyer, Excited-state decay pathways of tris(bidentate) cyclometalated ruthenium(II) compounds, Inorg. Chem. 56 (2017) 13579–13592, https://doi.org/10.1021/acs.inorgchem.7b02321.
[70] K.T. Ngo, N.A. Lee, S.D. Pinnace, D.J. Szalda, R.T. Weber, J. Rochford, Probing the noninnocent π-bonding influence of N -carboxyamidoquinolate ligands on the light harvesting and redox properties of ruthenium polypyridyl complexes, Inorg. Chem. 55 (2016) 2460–2472, https://doi.org/10.1021/acs.inorgchem.5b02834.
[71] C. Yagüe, I. Echevarría, M. Vaquero, J. Fidalgo, A. Carbayo, F.A. Jalón, J.C. Lima, A.J. Moro, B.R. Manzano, G. Espino, Non-emissive Ru II polypyridyl complexes as efficient and selective photosensitizers for the photooxidation of benzylamines, Chem. – A Eur. J. 26 (2020) 12219–12232, https://doi.org/10.1002/chem.202001460.
[72] O.J. Stacey, S.J.A. Pope, New avenues in the design and potential application of metal complexes for photodynamic therapy, RSC Adv. 3 (2013) 25550, https://doi.org/10.1039/c3ra45219k.
[73] M. Li, R. Tian, J. Fan, J. Du, S. Long, X. Peng, A lysosome-targeted BODIPY as potential NIR photosensitizer for photodynamic therapy, Dyes Pigments 147 (2017) 99–105, https://doi.org/10.1016/j.dyepig.2017.07.048.
[74] X.-F. Zhang, X. Li, The photostability and fluorescence properties of diphenylisobenzofuran, J. Lumin. 131 (2011) 2263–2266, https://doi.org/10.1016/j.jlumin.2011.05.048.
[75] L. He, K.-N. Wang, Y. Zheng, J.-J. Cao, M.-F. Zhang, C.-P. Tan, L.-N. Ji, Z.-W. Mao, Cyclometalated iridium(III) complexes induce mitochondria-derived paraptotic cell death and inhibit tumor growth *in vivo*, Dalton Trans. 47 (2018) 6942–6953, https://doi.org/10.1039/C8DT00783G.
[76] J.-J. Cao, Y. Zheng, X.-W. Wu, C.-P. Tan, M.-H. Chen, N. Wu, L.-N. Ji, Z.-W. Mao, Anticancer cyclometalated iridium(III) complexes with planar ligands: mitochondrial DNA damage and metabolism disturbance, J. Med. Chem. 62 (2019) 3311–3322, https://doi.org/10.1021/acs.jmedchem.8b01704.
[77] C. Zhang, R. Guan, X. Liao, C. Ouyang, J. Liu, L. Ji, H. Chao, Mitochondrial DNA targeting and impairment by a dinuclear Ir–Pt complex that overcomes cisplatin resistance, Inorg. Chem. Front. 7 (2020) 1864–1871, https://doi.org/10.1039/D0QI00224K.
[78] E. Baggaley, J.A. Weinstein, J.A.A.G. Williams, Lighting the way to see inside the live cell with luminescent transition metal complexes, Coord. Chem. Rev. 256 (2012) 1762–1785, https://doi.org/10.1016/j.ccr.2012.03.018.
[79] X. Tian, Y. Zhu, M. Zhang, L. Luo, J. Wu, H. Zhou, L. Guan, G. Battaglia, Y. Tian, Localization matters: a nuclear targeting two-photon absorption iridium complex in photodynamic therapy, Chem. Commun. 53 (2017) 3303–3306, https://doi.org/10.1039/C6CC09470H.
[80] T. Kirchhausen, E. Macia, H.E. Pelish, Use of dynasore, the small molecule inhibitor of dynamin, in the regulation of endocytosis, in, Methods Enzymol. (2008) 77–93, https://doi.org/10.1016/S0076-6879(07)38006-3.
[81] D. van Straten, V. Mashayekhi, H. de Bruijn, S. Oliveira, D. Robinson, Oncologic photodynamic therapy: basic principles, current clinical status and future directions, Cancers (Basel) 9 (2017) 19, https://doi.org/10.3390/cancers9020019.
[82] R. Guan, L. Xie, T.W. Rees, L. Ji, H. Chao, Metal complexes for mitochondrial bioimaging, J. Inorg. Biochem. 204 (2020), 110985, https://doi.org/10.1016/j.jinorgbio.2019.110985.
[83] C. Caporale, M. Massi, Cyclometalated iridium(III) complexes for life science, Coord. Chem. Rev. 363 (2018) 71–91, https://doi.org/10.1016/j.ccr.2018.02.006.
[84] J.J. Hu, N.-K. Wong, S. Ye, X. Chen, M.-Y. Lu, A.Q. Zhao, Y. Guo, A.C.-H. Ma, A.Y.-H. Leung, J. Shen, D. Yang, Fluorescent probe HKSOX-1 for imaging and detection of endogenous superoxide in live cells and in vivo, J. Am. Chem. Soc. 137 (2015) 6837–6843, https://doi.org/10.1021/jacs.5b01881.
[85] L.D. Zorova, V.A. Popkov, E.Y. Plotnikov, D.N. Silachev, I.B. Pevzner, S. S. Jankauskas, V.A. Babenko, S.D. Zorov, A.V. Balakireva, M. Juhaszova, S. J. Sollott, D.B. Zorov, Mitochondrial membrane potential, Anal. Biochem. 552 (2018) 50–59, https://doi.org/10.1016/j.ab.2017.07.009.
[86] M. Ouyang, L. Zeng, K. Qiu, Y. Chen, L. Ji, H. Chao, Cyclometalated Ir III complexes as mitochondria-targeted photodynamic anticancer agents, Eur. J. Inorg. Chem. 2017 (2017) 1764–1771, https://doi.org/10.1002/ejic.201601129.
[87] Y. Li, K.N. Wang, L. He, L.N. Ji, Z.W. Mao, Synthesis, photophysical and anticancer properties of mitochondria-targeted phosphorescent cyclometalated iridium(III) N-heterocyclic carbene complexes, J. Inorg. Biochem. 205 (2020), https://doi.org/10.1016/j.jinorgbio.2019.110976.
[88] O. Haapanen, V. Sharma, Redox- and protonation-state driven substrate-protein dynamics in respiratory complex I, Curr. Opin. Electrochem. 29 (2021), 100741, https://doi.org/10.1016/j.coelec.2021.100741.
[89] H. Huang, S. Banerjee, K. Qiu, P. Zhang, O. Blacque, T. Malcomson, M.J. Paterson, G.J. Clarkson, M. Staniforth, V.G. Stavros, G. Gasser, H. Chao, P.J. Sadler, Targeted photoredox catalysis in cancer cells, Nat. Chem. 11 (2019) 1041–1048, https://doi.org/10.1038/s41557-019-0328-4.
[90] B. Van Houten, V. Woshner, J.H. Santos, Role of mitochondrial DNA in toxic responses to oxidative stress, DNA Repair (Amst) 5 (2006) 145–152, https://doi.org/10.1016/j.dnarep.2005.03.002.
[91] A. Kellett, Z. Molphy, C. Slator, V. McKee, N.P. Farrell, Molecular methods for assessment of non-covalent metallodrug–DNA interactions, Chem. Soc. Rev. 48 (2019) 971–988, https://doi.org/10.1039/C8CS00157J.
[92] J. Leal, L. Santos, D.M. Fernández-Aroca, J.V. Cuevas, M.A. Martínez, A. Massaguer, F.A. Jalón, M.J. Ruiz-Hidalgo, R. Sánchez-Prieto, A.M. Rodríguez, G. Castañeda, G. Durá, M.C. Carrión, S. Barrabés, B.R. Manzano, Effect of the aniline fragment in Pt(II) and Pt(IV) complexes as anti-proliferative agents. Standard reduction potential as a more reliable parameter for Pt(IV) compounds than peak reduction potential, J. Inorg. Biochem. 218 (2021), 111403, https://doi.org/10.1016/j.jinorgbio.2021.111403.
[93] J.L. García-Giménez, M. González-Alvarez, M. Liu-González, B. Macías, J. Borrás, G. Alzuet, Toward the development of metal-based synthetic nucleases: DNA binding and oxidative DNA cleavage of a mixed copper(II) complex with N-(9H-purin-6-yl)benzenesulfonamide and 1,10-phenantroline. Antitumor activity in human Caco-2 cells and Jurkat T lymphocy, J. Inorg. Biochem. 103 (2009) 923–934, https://doi.org/10.1016/j.jinorgbio.2009.04.003.
[94] Z.H. Siddik, Cisplatin: mode of cytotoxic action and molecular basis of resistance, Oncogene 22 (2003) 7265–7279, https://doi.org/10.1038/sj.onc.1206933.
[95] M. Kielbik, D. Krzyzanowski, B. Pawlik, M. Klink, Cisplatin-induced ERK1/2 activity promotes G1 to S phase progression which leads to chemoresistance of ovarian cancer cells, Oncotarget 9 (2018) 19847–19860, https://doi.org/10.18632/oncotarget.24884.
[96] E. Buytaert, M. Dewaele, P. Agostinis, Molecular effectors of multiple cell death pathways initiated by photodynamic therapy, Biochim. Biophys. Acta - Rev. Cancer 1776 (2007) 86–107, https://doi.org/10.1016/j.bbcan.2007.07.001.